From the: Institut für Schlaganfall-und Demenzforschung
Klinikum der Universität München, Großhadern
Ludwig-Maximilians-Universität zu München

Dissertation
zum Erwerb des Doctor of Philosophy (Ph.D.)
an der Medizinischen Fakultät der
Ludwig-Maximilians-Universität zu München

Holistic Three-dimensional Cellular Mapping of Mammalian Organs by Tissue Clearing Technologies

vorgelegt von:

Shan Zhao

aus:

Shijiazhuang, Hebei, China

Jahr:

2020

Mit Genehmigung der Medizinischen Fakultät der

Ludwig-Maximilians-Universität zu München

First supervisor: *Univ.-Prof. Dr. rer. nat. Jürgen Bernhagen*

Second supervisor*:* *Prof. Dr. Christian Haass*

Third supervisor: *Dr. Ali Ertürk*

Dean: **Prof. Dr. med. dent. Reinhard Hickel**

Datum der Verteidigung:

09.12.2020

AFFIDAVIT

Zhao, Shan

Name, Vorname

Ich erkläre hiermit an Eides statt,
dass ich die vorliegende Dissertation mit dem Thema

“Holistic Three-dimensional Cellular Mapping of Mammalian Organs by Tissue Clearing Technologies”

selbstständig verfasst, mich außer der angegebenen keiner weiteren Hilfsmittel bedient und alle Erkenntnisse, die aus dem Schrifttum ganz oder annähernd übernommen sind, als solche kenntlich gemacht und nach Herkunft unter Bezeichnung der Fundstelle einzeln nachgewiesen habe.

Ich erkläre des Weiteren, dass die hier vorgelegte Dissertation nicht in gleicher oder in ähnlicher Form bei einer anderen Stelle zur Erlangung eines akademischen Grades eingereicht wurde.

München, 09.12.2020 — Ort, Datum

Shan Zhao — Shan Zhao

TABLE OF CONTENTS

AFFIDAVIT 3
TABLE OF CONTENTS 4
ABBREVIATIONS 5
PUBLICATION LIST 6
INTRODUCTORY SUMMARY 7
1. Holistic Study of Organisms 7
1.1 Organism Mapping Programs 7
1.2 Implemented Technologies 8
1.2.1 Magnetic Resonance Imaging (MRI) 8
1.2.2 Anatomical Pathology 9
1.2.3 History of Histology 9
1.2.4 Omics 11
1.2.5 Deep Learning 12
2. Tissue Optical Clearing 12
2.1 Optical Properties of Tissue 14
2.2 How to Image Thick Tissue 15
2.3 Development of Tissue Clearing Technology 19
2.4 Current Application of Tissue Clearing 24
2.5 Current Challenge and Prospective of Tissue Clearing 25
3. Research Aims 30
4. Research Summary 31
PUBLICATION I 33
PUBLICATION II 34
ADDITIONAL CONTRIBUTIONS 35
Summary 35
Introduction 35
Results 36
Discussion 42
Materials and Methods 44
REFERENCES 50
ACKNOWLEDGEMENTS 64

ABBREVIATIONS

3D	Three-dimensional
HBP	Human Brain Project
CBRAIN	Canadian Brain Imaging Research Platform
MRI	Magnetic Resonance Imaging
SNR	Signal-to-noise ratio
IHC	Immunohistochemistry
GFP	Green fluorescent protein
DIC	Differential difference contrast
UV	Ultraviolet
FRAP	Fluorescence recovery after photobleaching
TIRF	Total internal reflection fluorescence
LSFM	Light-sheet fluorescence microscopy
SPIM	Single-plane illumination microscopy
RI	Refractive index
SEM	Scanning electron microscopy
THF	Tetrahydrofuran
BA	Benzyl alcohol
BB	Benzyl benzoate
FPs	Fluorescence proteins
DBE	Dibenzyl ether
ECi	Ethyl cinnamate
DCM	Dichloromethane
TDE	2,2'-thiodiethanol
CUBIC	Clear, unobstructed brain imaging cocktails and computational anslysis
MADA	m-xylylenediamine
SDS	Sodium dodecyl sulphate
CLARITY	Crosslinked to a three-dimensional network of hydrophilic polymers
ETC	Electrophoretic Tissue Clearing
GA	Glutaraldehyde
HCR	Hybridization chain reaction
ExM	Expansion Microscopy
EDC	1-ethyl-3-3-dimethyl-aminopropyl carbodiimide
EDTA	Ethylenediaminetetraacetic acid
PI	Propidium iodide
NA	Numerical aperture
FOV	Field of View
WD	Working Distance
OTLS	Open-top light-sheet
PP	poly(ethylene glycol)-poly(L-lysine)
FACS	Flow cytometry
Iba1	Ionized calcium binding adaptor molecule 1
PET	Positron emission tomography
C-DSLM	Low-cost cleared tissue digital scanned light-sheet microscopy
NeuroGPS	NeuroGlobalPostion-Systerm
VesSAP	Vessel segmentation and analysis pipeline
GPU	Graphical Processing Unit
AVV	Adeno-associated virus

PUBLICATION LIST

Shan Zhao, Mihail Ivilinov Todorov, Ruiyao Cai, Rami AI-Maskari, Hanno Steinke, Elisabeth Kemter, Hongcheng Mai, Zhouyi Rong, Martin Warmer, Karen Stanic, Oliver Schoppe, Johannes Christian Paetzold, Benno Gesierich, Milagros N. Wong, Tobias B. Huber, Marco Duering, Oliver Thomas Bruns, Bjoern Menze, Jan Lipfert, Victor G. Puelles, Eckhard Wolf, Ingo Bechmann, Ali Ertürk. Cellular and Molecular Probing of Intact Human Organs. ***Cell,*** 2020,180,1-17

Shan Zhao, Janye Dai, Mo Hu, Chang Liu, Rong Meng, Xiaoyan Liu, Chu Wang, Tuoping Luo. Photo-induced coupling reactions of tetrazoles with carboxylic acids in aqueous solution: application in protein labelling. ***Chem. Commun.***, 2016,52,4702-4705

Shan Zhao, Zhiyuan Shen, Jingyu Wang, Xiaokang Li, Yang Zeng, Bjingjie Wang, Yonghong He, Yanan Du. Glycerol-Mediated Nanostructure Modification Leading to Improved Transparency of Porous Polymeric Scaffolds for High Performance 3D Cell Imaging. ***Biomacromolecules***, 2014,15, 7,2521-2531

Shan Zhao, Hui Zhao, Xinyong Zhang, Yaqian Li, Yanan Du. Off-the-shelf Microsponge Array for Facile and Efficient Construction of 3D Cellular Microenvironment. ***Lab Chip***, 2013,1**3**,2350-2358

Ruiyao Cai*, Chenchen Pan*, Ghasemigharagoz A, Todorov MI, Forstera B, **Zhao S**, Bharia HS, Mrowka L, Theodorou D, Rempfle M, Xavier A, Kress BT, Benakis C, Liebscher S, Liesz A, Menze B, Kerschensteiner M, Nedergard M, Erturk A. Panoptic imaging of transparent mice reveals whole-body neuronal projections and skull-meninges connections, ***Nature Neuroscience (cover)***, 2019,22,317–327

Lu Y, **Zhao S**, Zhou S, Chen SC, Luo T. Enantioselective syntheses and application of 4-epi-galiellalactone and the corresponding activity-based probe: from strained bicycles to strained tricycles, ***Org. Biomol. Chem.,*** 2018,17(7):1886-1892

Dai J, Liang K, **Zhao S**, Jia W, Liu Y, Wu H, Lv J, Cao C, Chen T, Zhuang S, Hou X, Zhou S, Zhang X, Chen XW, Huang Y, Xiao RP, Wang YL, Luo T, Xiao J, Wang C. Chemoproteomics reveals baicalin activates hepatic CPT1 to ameliorate diet-induced obesity and hepatic steatosis, ***Proc Natl Acad Sci USA***. 2018,115(26):E5896-E5905

Xuerong Yu, Fan Su, Chang Liu, Haosen Yuan, **Shan Zhao**, Zhiyao Zhou, Tianfei Quan, Tuoping Luo. Enantioselective Total Syntheses of Various Amphilectane and Serrulatane Diterpenoids via Cope Rearrangements, ***J Am Chem Soc***. 2016,138(19):6261-70.

Zhao H, Li X, **Zhao S**, Zeng Y, Zhao L, Ding H, Sun W, Du Y. Microengineered *in vitro* model of cardiac fibrosis through modulating Myofibroblast Mechanotransduction, *Biofabrication*. 2014, 6(4):045009

Li X, Zhang X, **Zhao S**, Wang J, Liu G, Du Y. Micro-scaffold Array Chip for upgrading cell-based High-throughput drug testing to 3D using benchtop equipment, ***Lab Chip.*** 2014,14(3):471-81

Chen H, Zeng Y, Liu W, **Zhao S**, Wu J, Du Y. Multifaceted applications of nanomaterials in cell engineering and therapy. ***Biotechnol Adv***. 2013,31(5):638-53

INTRODUCTORY SUMMARY

1. Holistic Study of Organisms

Living organisms granted by nature are incredible and complex symphony with trillions of cells and surrounded extracellular matrix. These cells are organized in different levels of spatial scale and driving multitude of functions in both physiology and pathology states. While modern biology and modern medicine already know the fundamental resident component of cells inside of most organs and their interactions with exogenous substances (e.g. drug, virus, nanomaterial etc.), holistic understanding and studying committed to cellular and molecular interrogations across the whole organisms are still missing. A systematic three-dimensional (3D) map annotated with various cell types, in addition to cell-cell and cell-matrix interactions in the native niche of organisms would greatly enhance our understandings of normal function, natural development and aging, disease progression, as well as the outputs of medicine delivery (**Figure 1**).

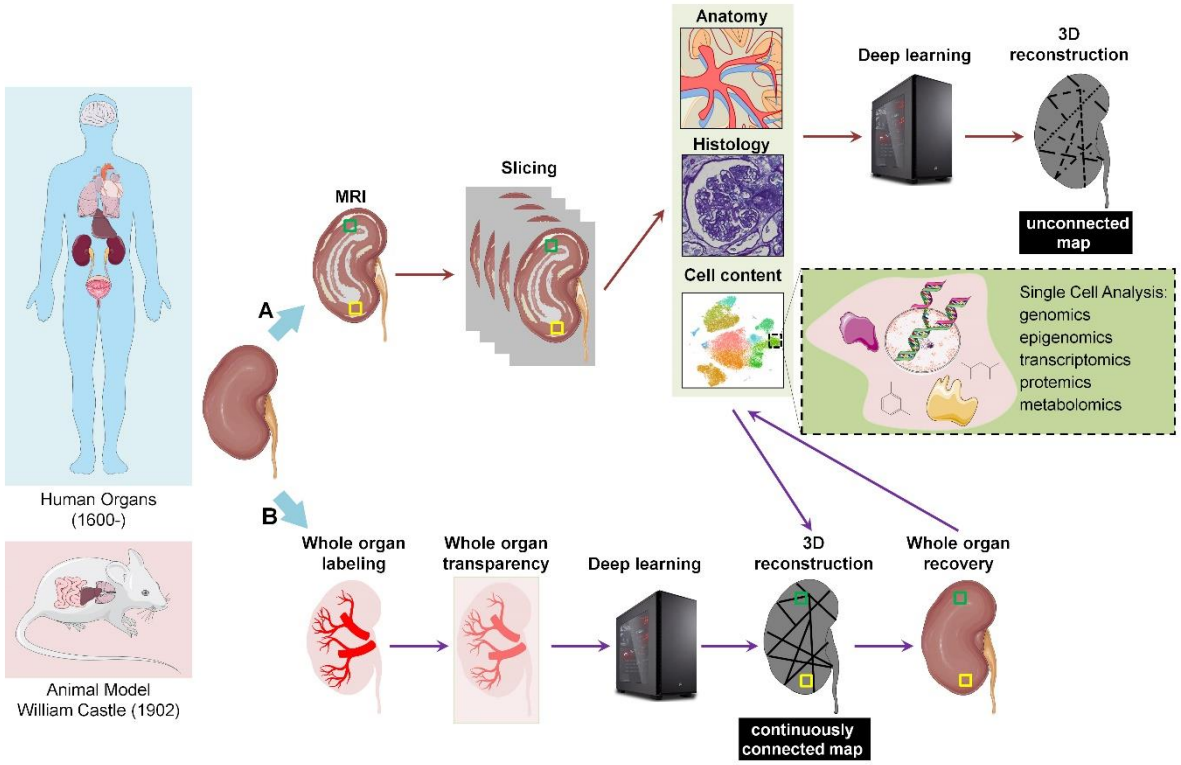

Figure 1. Organism 3D map generation and registration across cellular and spatial scales
Atlas of organism (human or rodent) with single cell content could be generated by implemented technologies including tranditional MRI, Anatomy, Histology and state-of-the-art 'Omics', Tissue Clearing and Deep Learning. **B** pipeline would provide continuously connected map comparing to **A** pipeline benifiting from the tissue clearing technology.

1.1 Organism Mapping Programs

Recently, organ-mapping initiatives have been booming around the world, collecting multidisciplinary knowledge and coordinating scientists in a global push to fully understand the organisms. The Human Protein Atlas[1] aims to generate a full map covering all proteins inside of human cells, tissues and organs to provide an open-resource for academia and industry.

The HPA was first reported in 2003 by Swedish (*https://www.proteinatlas.org/*). The European Union's flagship 'Human Brain Project (HBP, *https://www.humanbrainproject.eu/en/*)' is a 10-year project starting in 2013 and involving more than 500 scientists to study the basic science of how the brain works. In 2015, 'Canadian Brain Imaging Research Platform (CBRAIN)[2]' was developed as a web portal to provide tools to overcome the large-scale data processing challenges of neuroimaging. Another collaborative community of world-leading scientists built the 'Human Cell Atlas[3] (*https://www.humancellatlas.org/*)' in 2016, with the purpose of establishing reference maps as elaborate as carrying specific ID card of each cell and allowing to identify the ones associated with disease comparing with health to provide insights during the diagnosing and treating processes. Other running initiatives include Life Time (*https://lifetime-fetflagship.eu/*), consortiums funded by NIH targeting to specific organs such as lung (*https://www.lungmap.net/*), tumors (*https://humantumoratlas.org/*), genitourinary (*https://www.gudmap.org/*), kidney (*https://kpmp.org/about-kpmp/*) and so on. Especially, October of 2019, HuBMAP[4] was released as a NIH sponsored program to provide web-based guidance and supporting technologies with the goal of mapping the human body at cellular level and creating comprehensive maps for different tissues (*https://commonfund.nih.gov/hubmap*).

1.2 Implemented Technologies

To achieve such long-term and knowledge-wide projects, researchers with diverse expertise should work together to integrate features of single cell into the high-content and high-resolution 3D map of tissue. The involved subjects could be anatomy, molecular biology, clinical, pathology, cellular biology, computational biology, developmental, biomedical engineering, data processing, software engineering and so on. At the same time, generation of such maps relies on transformative technologies, which are listed as following.

1.2.1 Magnetic Resonance Imaging (MRI)

Building on studies of Lauterbur[5] and Mansfield[6], who applied position-dependent magnetic field (gradient) to reconstruct the spatial distribution of nuclear spins within 2D image slice, magnetic resonance imaging was invented and introduced into clinical use in the early 1980s. They also shared the Nobel Prize in Medicine in 2003. The MRI technology, as one of the most important *in vivo* diagnose methods in an invasive way, could depict a variety of anatomical regions of tissue and answer amount of morphological and functional questions[7-11]. For example, functional MRI and diffusion-weighted MRI are already respectively applied to infer the functional and structural connectivity of human brain for mapping and annotating human connectomes with cognitive and behavioral associations[12]. However, the big and fundamental limitation of the technique is the low sensitivity of signal-to-noise ratio (SNR) with corresponding low spatial resolution. Even using 'ultra-high field' of 7 Tesla MRI scanner, the

spatial resolution of *ex vivo* whole human brain is about 100 nm[13,14], 10 times bigger than single cell resolution. To effectively navigate the 3D organs, MRI images could help to identify marks based on the gross view of intact organs and guide towards 3D construction.

1.2.2 Anatomical Pathology

Anatomy is the study of the structures of body, pathology is the study of the functions of body, and anatomical pathology focuses on the study of tissues removed from a living or dead person to diagnose diseases or causes of death. Anatomical and pathological examinations represent very traditional methods originated from ancient cultures and still play important roles in modern medical and clinical researches, which observe the human tissue and body by surgery or autopsy to assist disease diagnoses and to evaluate therapeutic effects. Gross or macroscopic anatomy mainly observes large structures visible to the naked eye such as kidney, lung and heart. Microscopical anatomy deals with small structures to be examined by microscope. The investigation includes specific characterizations[15] of: i) single cells with the focus of morphologic features related to the color, integrity, texture and cytoplasm; ii) the patterns of cell accumulations presenting as clusters, tubular, sheets, or gland-like structures; iii) the tissue niches where the cells interact with the non-cellular components characterized with invasion, fibrosis, necrosis, or microcalcification. This subdivision of collecting abundant cellular and molecular information of tissue is normally considered as histology, which is still taken granted as the gold standard technique[16].

1.2.3 History of Histology

With the invention of microscope in 1591 by Zacharias Janssen[17,18], for the first time, scientists could observe microstructures even inside tissues and cells such as the mitochondria, other organelles, cytoplasm and so on. The routine techniques have been established in research laboratories covering the sectioning, staining and imaging steps with the standard examples of immunohistochemistry (IHC), vibratome, cryostats and fluorescence microscope.

Sectioning Techniques

Microtechniques for tissue sectioning developed with the mechanical devices, microtomes. The prototype hand-held microtome was invented by Hill in 1770[19], which was thought to be the so-called ‘cutting engine’. During the nineteenth century, only three main types of microtomes are longstanding[20]: a) the rocking microtome made in Cambridge; b) the Thoma-Jung sliding microtome; c) the Minot rotation microtome. Moreover, freezing microtome was developed for the preparation of frozen tissue sections in 1870. For fresh or fixed specimens without freezing or embedding, tissue chopper and vibratome[21] existed to prepare sections with 10-1000 μm thickness. Since 1939, there is also ultramicrotomy for cutting sections in the order of 50-100 nm thickness to study the fine structure of cells by electron microscopy. The

techniques of microtome allow the inner part of tissue getting exposure to researchers and help to form the fundamental theories about how tissue is composed and could be functioning.

Staining Techniques History

The initial historical staining works done by Leeuwenhoek[22] in the seventeenth century were adopted by pathologists and surgeons at the beginning, where substances found in nature were simply used to stain tissues like Madder, indigo and saffron, together with simple microscopes were used to study them after staining. In 1858, Joseph Von Gerlach[23,24] successfully stained cerebellum cells with ammoniacal carmine and he was widely regarded as the founder of microscopical staining. Later by testing various dyes made for textile industry[25], there are some important dyes are extremely versatile and used in the past and present for staining tissues, including carmine[26], hematin and hematoxylin[27] and silver nitrate[28]. The development of modern immunohistochemistry have been greatly promoted by the discovery of antibody[29] in early 1900s, an approach in which antibodies could specifically recognize antigens' sites inside tissues by lock-and-key structure binding interaction[30]. There are two subtypes of antibody labeling methods. One type is that the antibody chemically conjugated fluorochrome could label antigens in the tissue frozen section as a 'direct approach'[31] and it was firstly demonstrated by Coons, Creech, and Jones in 1941. But this process requires abundant primary antibodies. So, 'indirect immunolabeling' is developed involving a two-step protocol of using primary antibody to target the tissue antigen and using another antibody tagged with fluorochrome to target the primary antibody (called secondary antibody)[32]. The secondary antibody could be modified with amounts of different commercialized and cheap fluorophores. Reported works have applied multiplex immunohistochemistry on a given single tissue to detect multiple antigens and generated muilticolor pictures from differential labeling[33].

The use of animals as models of human anatomy and physiology began in ancient Greece. The selection of animal model with most informative species is very important considering of experimental and financial feasibility, biological characteristics, and the available palette of imaging and molecular techniques. Among of zebrafish, pig, rat, drosophila, mice helped researchers worldwide and contributed to 17 Nobel Prizes[34]. In 1909, Clarence Cook Little[35] found the Jackson Laboratory and created the first inbred mice stain. With the discovery of green fluorescent protein (GFP)[36], Masaru Okabe[37] generated the transgenic mouse expressing GFP in 1997, which was called Green mouse. Since then, reporter mice lines[38] have become widely used in research to visualize the *in vivo* cell characteristics by expressing fluorescent proteins across spectral variants of GFP, with most cases of checking certain gene expression, identifying the locations of subtype cellular structures or monitoring the progression of cell cycles. Recently, multi-color imaging of cells in one mouse line using

designable *Brainbow* technology [39] or spatiotemporal gene expression controlled by photoactivatable Cre technology[40] represent cutting-edge fluorescent labeling technologies.

Imaging techniques

After the invention of microscope by Zacharias Janssen and his son Hans Janssen, Antonie Van Leeuwenhoek[41] (1632-1723) and Robert Hooke[42] (1635-1703) respectively developed lens microscope and compound microscope in order to investigate microorganisms like bacterial cells or common fly. Over a period of decades, scientists were attracted by the compound microscope, until 1897, when the stereomicroscope was made by Zeiss company and allowed three dimensional views of tissue[43]. One of the challenges in imaging cultured cells is their inherently low contrast caused by the similar refractive index between cells and culture medium. During the nineteenth century, Fritz Zernike invented phase contrast microscopy and won the Nobel Prize in 1953[44,45]. For unstained samples, Smith[46] and Georges Nomarski[47] introduced the differential interference contrast (DIC) technique in 1955 that was taken as the current standard method to increase the contrast. Besides, the advent of fluorescent dyes or proteins also revolutionize the contrast with the construction of fluorescence microscope, which originally is ultraviolet (UV) microscopy developed by August Köhler in 1904[48]. After the introduction of dichroic mirrors since 1967[49], diverse innovative illumination modes have been applied, for instance fluorescence recovery after photobleaching (FRAP), two-photon, total internal reflection fluorescence (TIRF), confocal and light sheet fluorescence microscopy (LSFM)[50]. Specially, LSFM typically has the advantage of allowing relatively higher resolution imaging (several micrometers of subcellular level) with faster speed by illuminating the labeled tissue with a thin plane sheet of light. The first reported LSFM in 1903[51] was a very simple version, where gold particles were irradiated with the sunlight through a aperture projection process. It is until 2004 Huisken Jan described single-plane illumination microscopy (SPIM) in *Science*, the development and use of LSFL were greatly accelerated[52,53].

1.2.4 Omics

Omics studies refer to topics of biological sciences with the ending of –omics, including genomics, epigenomics, transcriptomics, metabolomics or proteomics, which target to identify, characterize and quantify all biological molecules inside of a cell, tissue or organism involving in the structure, function and dynamics[54,55]. The multitude of genes, RNAs, proteins or metabolites in a single omics technique or combinations of omics techniques generate a vast amounts of data, require enable resources or tools to understand the correlations and dependencies of molecular components with high sensitivity and specificity at a systemic level[56,57]. For example, the Wellcome Trust Sanger Sequencing Centre now achieves thousands of millions of production of base pairs in a robust and cost-efficient way each day. Bioinformatics rely on computer programs, mathematical formulas and statistical measures to

process extensive analyses in forms of searching in biological databases or grouping the data with molecular patterns to identify prominent elements between diseased and healthy phenotypes[58,59]. The general pipeline includes: a) processing original data to identify the underline molecules, b) statistical analysis of molecular information with significances, c) mapping the connected pathway based on databases, d) generating models from a systematic context view. Omics have contributed widely to explain the delicate physiologic equilibrium and expanded to combine with single cell clustering[60-62], deep learning-based analysis[63,64], will eventually aid the development of measures for disease prevention, diagnosis, monitoring and treatment.

1.2.5 Deep Learning

As one representative branch of machine learning methods, deep learning is based on artificial neural networks, which starts from inputting raw data into a machine, allows to generate learnt patterns and to automatically and predictably discover representations on future unseen data[65,66]. In the last years, it already showed big advantages in dealing with high-dimensional data, therefore being widely applied in academy, business to government. For example, deep learning methods have proven to give outstanding outcomes in the field of drug discovery[67,68], image recognition and analysis[69-71], visual art[72], bioinformatics[73-75] with very little engineering by hand. The artificial neural networks are designed to mimic the human brain, presenting as a collectively connected web of nodes or units. Different with traditional problem-solving in a linear way, deep learning methods process data in a nonlinear approach at hierarchical level. Among the three types of learning paradigms of supervised learning, reinforcement learning and unsupervised learning, the most used form is supervised learning, in which collected large paired input data were trained to give desired outputs described as scored vectors for each input. To minimize the error between tested output scores and the final desired scores, internal adjustable parameters, also called weights, are set and modified to refine the input-output feedback functions of the system. When referring to analyze fluorescent colorful images, convolutional neural networks are commonly built to process pixel intensity data from each individual channel that originally composing by 2D arrays[71]. In summary, to analyze the large sets of unstructured data in each group of cellular information of anatomy, histology or cell content coming from thousands of sections of full organ, deep learning solutions using a machine could represent promising and efficient ways comparing to using decades of human work.

2. Tissue Optical Clearing

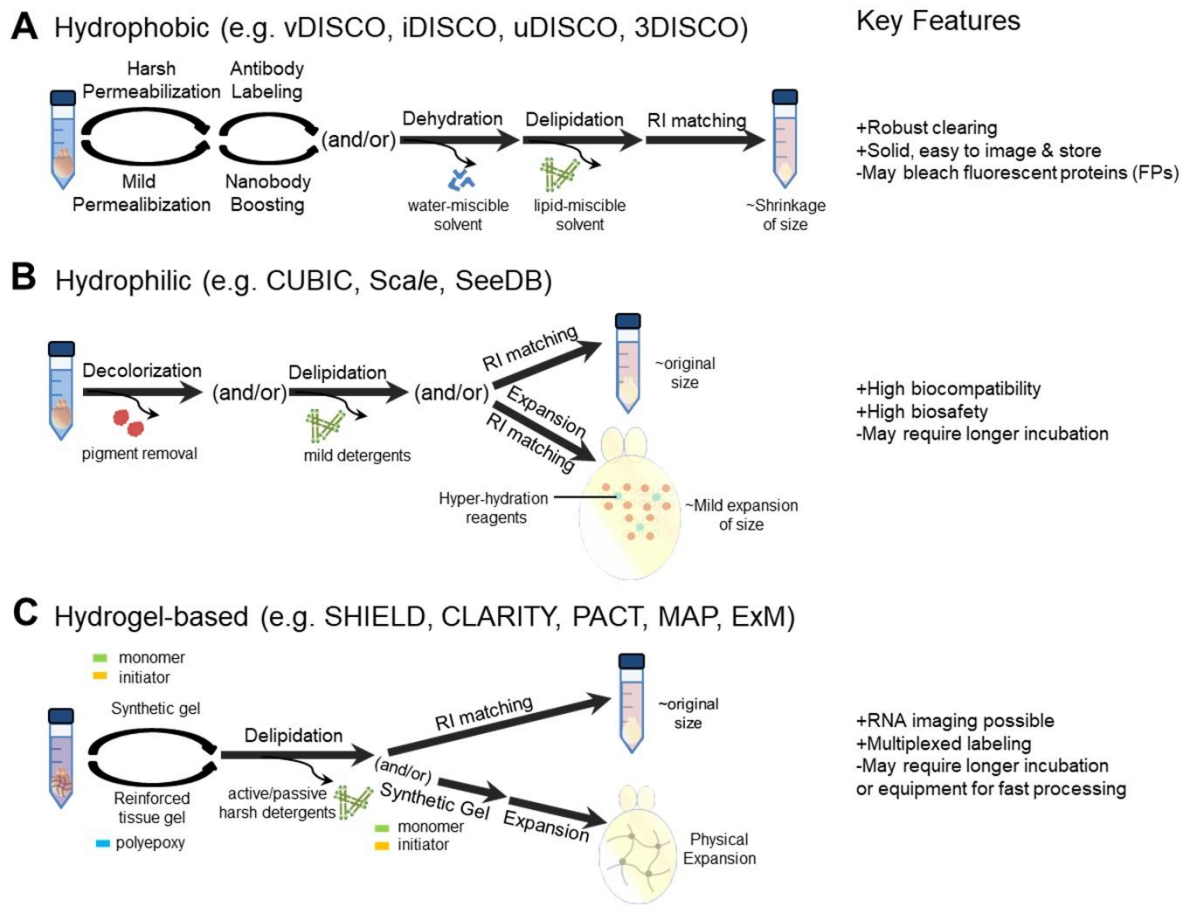

Figure 2. The general processes and key features of three types of tissue clearing technologies.
A. Hydrophobic solvent based tissue clearing method representing by vDISCO, iDISCO and so on mainly includes permeabilization, labeling, dehydration, delipidation and RI (refractive index) matching steps. **B**. Hydrophilic solvent based tissue clearing method uses water solvable reagents to decolorize the pigments or mild detergents to delipid before RI matching to well preserve transgenic fluorescence, such as CUBIC, SeeDB. **C.** Hydrogel based tissue clearing method introduces polymer network inside of tissue to support stronger delipidation treatments before RI matching, including SHEILD, CLARITY.

For the last decades, optical imaging methods including confocal microscopy, super resolution microscopy, multiphoton microscopy, stereomicroscopy, and light-sheet microscopy play vital roles in the physiological and biological researches since they provide accurate and informative microstructural features of tissue in a simple and safe way. However, body tissues are mainly composed of water, lipid, protein, carbohydrate and ash contents[76], which cause prominent light scattering and absorption across tissue different layers and result in lower contrast and poorer spatial resolution to distinguish neighboring spots, as well as limited imaging depth in optical imaging techniques. Tissue optical clearing mechanism is based on the refractive index (RI) matching between tissue immersion solution and tissue components, before which interested proteins are crosslinked for retention but light scatters like lipid and light absorbers like heme are removed by chemicals[77]. Pioneered by Werner Spalteholz since 1914, three kinds of tissue clearing technologies have been developed including hydrophobic solvent-based clearing, hydrophilic reagent-based clearing and hydrogel-based clearing to systematically understand the structural and molecular functions of animal and human clinical specimen[78] (**Figure 2**).

2.1 Optical Properties of Tissue

During optical imaging process, the light irradiated to the observing tissue has to penetrate across the tissue surface, interrogate with the variable components inside of tissue, then escape out from the tissue for detection. Accordingly, there are two main principle interactions between the light and the tissue, absorption and scattering[79]. A fundamental understanding of the origins of light absorption and scattering is a key to properly design optical imaging system, interpret imaging results or plan tissue clearing protocols. Structurally, tissue comprises of different cell types, vasculatures, connective fibers, and a complex mesh of extracellular matrix. Chemically, molecules including proteins, lipids, water, carbohydrate distribute across different spatial scales formed all structures. On the other hand, light could be modeled as a wave or discrete photons. In the end, the intrinsic interactions between the light and the tissue are the interactions between photons and tissue molecules.

Light absorption would happen when the energy of light (also refer to photon frequency) is taken up by a molecule that needed for its energy transition. The tissue molecules are simply chemical compounds. As described by Textbook of Engineering Chemistry (4^{th} edition): “chemical compounds present various sorts of orbitals showing relative energies: σ (bonding), π (bonding), n (non-bonding), π* (anti-bonding) and σ* (anti-bonding). When a photon passes through the compound, energy of the light would promote an electron to jump from the low energy level of bonding or non-bonding orbital into the high energy level of empty anti-bonding orbitals. Each wavelength of light has a specific associated energy, only when this specific energy reaches the right amount for promoting one type of energy jumps, immediately this wavelength light would be absorbed by the compound. In the general microscopy imaging range of near ultra-violet to very near infra-red spectrum (200 nm-800 nm), three possible electron jumps will happen after absorbing light in that region: i) from π (bonding) orbitals to π* (anti-bonding) orbitals; ii) from n (non-bonding) orbitals to π* (anti-bonding) orbitals; iii) from n (non-bonding) orbitals to σ* (anti-bonding) orbitals. Accordingly, we could see that compounds containing π bonds or carrying atoms of n non-bonding orbitals could absorb light of 200-800 nm. Typically, the absorption peak for π →π* jump is 180 nm and the absorption peak for n→ π* jump is 290 nm, so they are out of the microscopy imaging spectrum and these kinds of absorption could be fairly neglected. Some molecules have conjugated double bonds, which cause delocalization of the continuous π boding orbitals across the whole molecule. Absorption of these molecules requires less energy following the increased amount of delocalization effects and the maximum absorption moves to longer wavelengths to be in the visible region.” These molecules are the dominant absorbers or chromophores of the tissue contributing to the overall absorption in visible spectrum for microscopy imaging, such as

hemoglobin, myoglobin, melanin and flavoproteins[80]. The absorption properties of tissue could be understood as the superimpose of individual chromospheres in a linear way.

Light scattering would occur whenever the light falls through a change of medium with different refractive index, in the case of tissue probing, such as the presence of heterogeneities of water, lipid and protein. According to the book of Optics (Hecht Eugene, 2002), “refractive index is defined as the velocity ratio of specified wavelength light between vacuum and examined substance.” When the photon hits on a substance (a particle or a molecule), and thereby changes its direction, light scattering happens. If the incident photon could change direction but do not change their wavelength or frequency without loss of energy, this process is called elastic scattering (e.g. Rayleigh scattering, Mie scattering)[81]. If a fraction of vibrational energy of incident photon is lost or gained by the molecule or particle, there is a shift in wavelength or frequency of incident photons, this process is called inelastic scattering (e.g. Stokes Raman scattering, anti-Stokes Raman scattering)[81]. The elastic scattering of light is the most important interaction of light-tissue. As we known, it is not feasible to exactly descript the spatial distribution of different tissue molecules at the nanometer level with detailed knowledge of each respective refractive index, in hence the scattering properties of tissue is extremely complex and challenging to evaluate quantitatively. However, many studies have characterized the refractive index of common cell components. For example, the water sharing ~70-80% of tissue content has the refractive index of 1.33; the protein sharing ~10% of tissue content has the refractive index of 1.50; the lipid sharing ~10% of tissue content has the refractive index of 1.48. Other contents are listed as: melanin, 1.7; cytoplasm, 1.35-1.37; mitochondria, 1.42[82]. Scattering coefficient, μ_s, is commonly used to descript the cross-sectional scattering in volume or tissue level. Along the tissue thickness *dl*, the quantity light scattering is estimated as $\mu_s \times dl$[82]. Once the tissue is thick enough containing trillions of heterogeneous scatters, most of the incoming light would be scattered in every direction and the whole tissue will behave as if it contains multitude of weak luminous sources, therefore little light photons could be detected, rendering the opacity of tissue. In principle, a molecule of tissue of any size of any refractive index may give rise to the scattering of light.

2.2 How to Image Thick Tissue

Biological organs are opaque for optical imaging. Sectioning of organs into series of thin slices (several to dozens of micrometers) represents the typical and standard way to collect two-dimensional cellular information under microscopy and exerts laborious burdens for researchers since the process is time-consuming, repetitive and error-prone. Recently, more and more biological studies require 3D volumetric imaging of organs to reconstruct *in vivo* inherent 3D structural niches, especially, in neuroscience the nervous projections are the most

important but obvious examples, given that individual neurons have profusely branched axons extruding from the soma and extend a few hundred micrometers to many directions. In this case, thin sections of tissue cannot provide fully depiction of its nature morphology. Moreover, developmental biology needs to record the morphological changes of organs in 3D. To avoid the technically pitfalls of loss, distortion, fold, compress or stretch caused by serial thin section using microtome and corresponding unsatisfied 3D reconstruction due to imperfect sections, the possibility is combining the imaging and the microtome procedures together to generate the serial sectioning and scanning under sufficient control. Accordingly, serial block-face microscopy is emerging as a new technology: scanning electron microscope (SEM)[9] or light microscope[83,84] is specially designed to only scan the exposure surface part of specimens after integrated to either 1) a built-in ultramicrotome, which could cut off successively imaged layers, or 2) a focused ion beam which could sputters successively imaged layers. Such 'blockface' methods could address the inconnectivity or misalignment issues of traditional sections but at the expense of shaving off the imaged surface and destroying the specimen to exposure the next block surface. This means the whole process of imaging one tissue sample has to be conducted only one time and has to be running well without any accident, as well as, the tissue cannot be available for other experiments anymore. These technologies are promising in researches of using animal models like mice or rat with a large amount of populations at lower costs, yet not proper for studies of using human organs or biopsy.

Non-sectioning approaches came out to be a revolution of 3D volume imaging of tissues at cellular level and excited many research areas with the development of laser-scanning microscopes, especially multiphoton microscopy or light-sheet microscopy. For example, two-photo microscopy relies on that two photons from longer wavelength simultaneously shoot on the same molecule and added energies of two photons would induce the excitation state of the molecule[85]. This allows low-energy infrared photons as the hitting photons, which are less damaging and penetrate more deeply in tissue. Still, two-photon microscopy reaches maximum 500 -800 μm depth of tissue, hence, not be capable to image most intact organs[86]. Light-sheet microscopy (once termed 'ultramicroscopy') is based on light sheet illumination originally proposed 100-years ago[51]. In the design, two thin counterpropagating sheets of laser light from both sides are generated to illuminate on the specimen to image one layer of specimen. Other layers of the specimen except for the irradiating single plane are still in dark and this will avoid unfocused imaging[87]. However, light-sheet microscopy obviously was designed for optically transparent objects. Therefore, it is highly necessary to develop a technology to render biological tissues transparent.

Table 1 Summarized characters of three types tissue clearing technologies

Tissue clearing	Protocol	Fixation	Permeabilization	Decolorizing/ Bleaching	Dehydration	Delipidation	RI matching	Final RI	FP friendly	Immunostaining compatible	Process time	Process mode	Tissue morphology	Reference
hydrophobic-solvents based	Dodt; Jährling	PFA	/	/	ethanol/hexane	/	BABB	1.55	half day	/	> 9 days	incubation	shrinkage	Dodt et al. 2007; Jährling et al. 2009
	3DISCO; Becker; RetroDISCO	PFA	/	/	THF	DCM	BABB/DBE	1.56	1-2 days	yes	1-2 days	incubation	shrinkage	Ertürk et al. 2012; Becker et al. 2012; Zygelyte et al. 2016
	iDISCO	PFA	methanol/DMSO/NP40	H_2O_2	THF	DCM	DBE	1.56	/	yes	>20 days	incubation	shrinkage	Renier et al. 2014
	iDISCO+	PFA	methanol/DMSO	H_2O_2	methanol	DCM	DBE	1.56	/	yes	>20 days	incubation	original size	Renier et al. 2016
	uDISCO	PFA	/	/	*tert*-Butanol	DCM	BABB-D	1.56	> 1 month	yes	several days	incubation/ perfusion	shrinkage	pan et al. 2016
	sDISCO	PFA	/	/	purified THF	/	stabilised DBE	~1.56	22 months	/	> 5 days	incubation	shrinkage	Hahn at al. 2018
	FluoClearBABB; a-uDISCO	PFA	/	/	*tert*-Butanol/1-propanol in basic PH	/	BABB	1.56	many months	/	several days	incubation	shrinkage	Schwarz et al. 2015; Li et al. 2018
	Eci	PFA	/	/	ethanol (PH=9)	/	ethyl cinnamate	1.56	2 weeks	yes	1-2 days	incubation	shrinkage	Klingberg et al. 2016
	PEGASOS	PFA	/	Quadrol	*tert*-Butanol/PEG methacrylate/ Quadrol	*tert*-Butanol/ Quadrol	benzyl benzoate/PEGMMA500/ Quadrol	1,543	many months	yes	5-7 days	incubation/ perfusion	shrinkage	Jing et al. 2018
	FDISCO	PFA	/	/	THF (4°C, PH=9)	/	DBE	1.56	> 1 month	yes	3 days	incubation	shrinkage	Qi et al. 2019
	EyeCi	PFA	methanol/DMSO	10% Hydrogen peroxide	ethanol (PH=9)	/	ethyl cinnamate	1.56	/	yes	>7.4 days	incubation	original size	Henning et al. 2018
hydrophoilic-solvents based	Sca/e	PFA	urea/triton X-100/glycerol	/	/	/	urea/triton X-100/glycerol (Sca/eA2, Sca/eU2, AbSca/e)	~1.382	yes	yes	> 2 weeks	incubation	~1.25-fold expansion	Hama et al. 2011
	Ce3D	PFA	BD permeabilization buffer	/	/	/	N-methyacetamide/ Histodenz/ triton X-100/ thioglycerol	~1.5	yes	yes	3 days	incubation	/	Li et al. 2017
	Sca/eS	PFA	urea/triton X-100/sorbitol	/	/	/	urea/triton X-100/sorbitol (Sca/eS4)	1.44	yes	yes	several days	incubation	original size	Hama et al. 2011
	CUBIC; CB-perfusion	PFA	/	Quadrol	/	urea/Quadrol/triton X-100 (CUBIC1)	sucrose/urea/2,2',2'-nitrilotriethanol (CUBIC 2)	1.48–1.49	yes	yes	> 2 weeks	incubation/ perfusion	expansion	Susaki et al. 2014; Tainaka et al. 2014; Susaki et al. 2015
	CUBIC-cancer	PFA	/	N-buthyldiethanolamie	/	N-buthyldiethanolamie/ triton X-100 (CUBIC-L)	antipyrine/ nicotinamide (CUBIC-R)	1.52	yes	yes	10-16 days	incubation/ perfusion	expansion	Kubota et al. 2017
	CUBIC protocols	PFA	/	N-buthyldiethanolamie	/	1-methylimidazole/N-buthyldiethanolamie/ triton X-100 (CUBIC-P)	antipyrine/ N-methylnicotinamide / N-butyldiethanolamine (CUBIC-RA)	1.52	yes	yes	5-16 days	incubation/ perfusion	expansion	Tainaka et al. 2018
	SeeDB	PFA	/	/	/	fructose	fructose/α-thioglycerol	~1.49	yes	yes	several days	incubation	original size	Ke et al. 2013
	Clear$^{T/T2}$; RFI	PFA	/	/	/	formamide	formamide/PEG	~1.44	yes	yes	several days	incubation	original size	Kuwajima et al. 2013; Yu et al. 2018
	FocusClear	PFA	triton X-100/RNase A	/	/	/	FocusClear	1.47	yes	yes	several days	incubation	/	Liu et al. 2003
	FRUIT	PFA	fructose/urea	/	/	/	fructose/urea	~1.48	yes	yes	several days	incubation	original size	Hou et al. 2015
	TDE	PFA	2,2'-thiodiethanol	/	/	/	2,2'-thiodiethanol	1.42	yes	yes	days-weeks	incubation	/	Aoyagi et al. 2015; Staudt et al. 2007; Costantini et al. 2015; Musielak et al. 2016

	FOCM	PFA	/	/	/	/	urea/D-sorbitol/glycerol/DMSO	1.495	yes	yes	several minitues	incubation	~original size	Zhu et al. 2019
	MACS	PFA	sorbitol/m-xylylenediamine	/	/	/	sorbitol/m-xylylenediamine (MACS R2)	1.51	yes	yes	2.5 days	incubation	~original size	Zhu et al. 2019
	FlyClear	PFA	proteinase/aceton	THEED/Urea/triton X-100	/	/	Meglumine diatrizoate	1.45	yes	/	days-weeks	incubation	/	Pende et al. 2018
	UbasM	PFA	Meglumine/Urea/1,3-Dimethyl-2-imidazolidinone/Triton X-100	/	/	/	Urea/1,3-Dimethyl-2-imidazolidinone/ Sucrose	1.47–1.48	yes	yes	days-weeks	incubation	original size	Chen et al. 2017
	CUBIC-X expansion	PFA	/	Quadrol	/	urea/Quadrol/triton X-100 (CUBIC1)	imidazole/antipyrine (CUBIC X1, CUBIC X2)	1,467	yes	yes	weeks	incubation	10-folds expansion	Murakami et al. 2018
hydrogel based	**CLARITY**	PFA/acrylamide hydrogel	/	/	/	sodium dodecyl sulphate/boric acid	FocusClear/ glycerol	~1.47	yes	yes	> 7 days	electrophoresis	expansion	Chung et al. 2013; Tomer et al. 2014; Magliaro et al. 2015
	EDC-CLARITY	acrylamide/ EDC	/	/	/	sodium dodecyl sulphate/boric acid	FocusClear/ glycerol	~1.47	yes	yes	> 7 days	electrophoresis	expansion	Sylwestrak et al. 2016
	PACT	PFA/acrylamide hydrogel	/	/	/	sodium dodecyl sulphate	Histodenz/sodium azide/tween-20 (RIMS)	1.46	yes	yes	days-weeks	incubation/ perfusion	expansion	Yang et al. 2014; Treweek et al. 2015; Woo et al. 2016; Neckel et al. 1026
	SWITCH	glutaraldehyde	/	/	/	sodium dodecyl sulphate/hyroxide/boric acid/sodium sulfite	iohexol/ diatrizoic acid/ N-methyl-d-glucamine	147	yes	yes	days-weeks	incubation/ electrophoresis	expansion	Murray et al. 2015
	MAP	PFA/acrylamide hydrogel	/	/	/	sodium dodecyl sulphate	diatrizoic acid/N-methyl-d-glucamine/iodixanol	1.47	yes	yes	days-weeks	electrophoresis	expansion	Ku et al. 2016
	Expansion	acrylamide/N,N'-methylenebisacrylamide	/	/	/	Proteinase K	water	1.33	yes	yes	days-weeks	incubation	4.5-folds expansion	Chen et al. 2015; Zhao et al. 2017
	SHIELD	PFA/polyglycerol 3-polyglycidyl ether	/	/	/	SDS/ sodium borate/ sodium sulfite	iohexol/ diatrizoic acid/ N-methyl-d-glucamine	1,458	yes	yes	> 7 days	electrophoresis	expansion	Park et al. 2018
	ACT-PRESTO	acrylamide	/	/	/	sodium dodecyl sulphate/boric acid	Histodenz/ sodium azide (RIMS)	1.46	yes	yes	1 day	electrophoresis	expansion	Lee et al. 2016

2.3 Development of Tissue Clearing Technology

Tissue clearing concept is derived from the developments of histology technique and preservation of biological samples. Retrospective to a century ago, people were already tried to keep biological samples in solid hydrophobic polymers like resin[88] or paraffin wax[89]. Since biological tissue contains around 70% of water, with which hydrophobic polymers do not mix, the tissue should be firstly dehydrated by a series of alcohol-water mixtures with increasing proportions of alcohol. Then the alcohol was removed by soaking the tissue in an organic solvent miscible with polymers. This bath is known as a clearing reagent because it renders tissue transparent. For example, xylene[90] has been widely used as a clearing agent, and now been substituted by less toxic chemicals such as Histolene or HistoClear. Such embedding polymers, however, are intrinsically fluorescent and are quite hard and hydrophobic to allow aqueous staining solutions penetration. Beside, these kind of organic clearing reagents quench most transgenic fluorescent protein signal.

Until the beginning of 20th century, Spalteholz[91] (1911) performed the first transparent anatomical specimens by embedding tissue into media of different refractive indices (n_D). He reported the basic steps of tissue clearing including fixation (e.g. formalin or paraformaldehyde), bleaching (e.g. hydrogen peroxide), dehydration (e.g. alcohol), RI matching (e.g. methyl salicylate, benzyl benzoate, wintergreen oil). Over the following 100 years, scientists tried to modify his method to avoid the necrosis of tissue and the formation of bubbles, but with limited success[92-96].

As the high popularity of fluorescent microscopy, especially light sheet fluorescent microscopy, and the powerful capacity of computer for big data acquisition, storage and analysis, several studies were attempted to revisit the tissue clearing technology proposed by Spalteholz. The fundamental mechanism of all tissue clearing techniques is based on equilibrating the refractive index of tissue components across the whole organs and surrounding medium to decrease the inhomogeneity of light scatters, then the vast majority of fluorescence light photons could go through the tissue and get detected by the imaging system.

Hydrophobic solvent-based clearing technology

Hydrophobic solvent-based clearing methods follow the described steps from Spalteholz using organic solvents, which are mostly comprised of four steps: fixation, dehydration, delipidation and RI matching. 1) The first step of tissue fixation is to preserve interested molecules of tissue to prevent autolysis or degradation for further studies. A number of fixatives have been used for decades, even over a century, for example formaldehyde (since 1859) or paraformaldehyde to crosslink the side chain amino groups with the formation of inter- or intra-molecular

methylene bridge. Although there are alcohol-based fixatives like Carnoy's and Methacarn to cause protein denaturation and coagulation, they are very little-used in current practice [97]. Typically, proteins (RI, n>1.45) are the main aim of studies, which should be preserved during clearing process. 2) The purpose of tissue dehydration is removing the water part of tissue, which possesses 70-80% of tissue content with the refractive index of 1.33. The water-miscible solvents should have smaller size and lower viscosity to rapidly travel into tissue and replace the water by diffusion. Classically, alcohols and tetrahydrofuran (THF) are chosen. After replacement of water, there are less hydrogen-bond networks from intracellular molecules since alcohols or THF cannot provide as more hydrogen bonding ability as water. Therefore, the tissues usually become shrunk and harder after dehydration. Some of the dehydration solvents also have some extent of lipid-solvating capacity. 3) Still, delipidation step is necessary for high-lipid content tissues like liver. Organic solvents are more powerful for dehydrated tissue, which are hydrophobic and miscible with lipids including triglyceride, cholesterol, phospholipid and unesterified fatty acid [98]. 4) The retained proteins are the dominant constituent of tissue after removing of water and lipid resulting a relatively homogenous scatters of tissue, which has a fairly higher refractive index of >1.5 due to the shrinkage. To equal the refractive index of dehydrated and defatted tissue with inner and surrounding medium, aromatic solvents are commonly used as the final matching solution to render the tissue transparent.

In 2007, Dodt [99] et al. reported the 3D visualization of neuronal network of whole mouse brain imaged by ultramicroscopy after tissue clearing, using a graded ethanol series and hexane for dehydration and BABB (benzyl alcohol (BA):benzyl benzoate (BB)=1:2) as RI matching solution. It came out this protocol cannot achieve enough transparency of myelinated and high-lipid tissues such as adult spinal cord and brain stem of rodents, in addition that quickly quench signal from the transgenic fluorescent protein (typically, green fluorescent protein, GFP). Extensive chemicals screening studies were performed to find better solvents for dehydration, delipidation and RI matching respectively (**Table 1**). With the emerging biotechnologies of genetically engineered mice [100] and fluorescence proteins (FPs) [101], transgenic mouse lines expressing fluorescent proteins provide valuable tools for studying human diseases. Most tissue clearing techniques focus on the preservation of proteinaceous fluorophores (XFPs), whose 3D configurations are sensitive to temperature [102], PH [102-106], and inert of surrounding chemicals [107]. Ethanol, THF[108-110] and *tert*-butanol [111] are found to be fluorescence protein-friendly dehydration solvents within short days, yet could stabilize fluorescent signal up to months in special conditions for example purified solvent [112], low temperature [102] (4°C) and basic environment (PH>9) [102-105]. DCM is firstly used as delipidation solvent in 3DISCO clearing protocol developed by Ertürk in 2012, which helps to clearing multiple organs with high lipid

content [109]. To date, all RI matching solutions have a refractive index of ~1.56 including BABB, dibenzyl ether (DBE) or ethyl cinnamate (ECi). Except the 3D volume image of transgenic fluorescent signal by tissue clearing techniques, traditional immunostaining methods using antibodies or small molecular dyes historically play vital roles in the molecular and cellular integrations of biological tissue. However, antibodies are big size (~150 kDa) proteins and cannot penetrate deeply into the tissue. Renier [113,114] et al. invented iDISCO protocol that achieved whole mouse brain antibodies immunolabeling after permeabilization using methanol/ Dichloromethane (DCM) or DMSO and bleaching using H_2O_2. This broadened the range of utility of tissue clearing to biological studies.

Hydrophobic solvent-based clearing technologies are easy-to-use, transformative, robust, and applicable to mouse organs (e.g. brain, spine cord, liver, spleen, liver, hear, bone, lung, gut etc.), even to intact adult mouse [111,115]. Passive incubations interweaving with exchange of solutions are the main laborious operations for mouse organs, which could be easily implemented in diverse labs. Isotropic shrinkage of cleared tissue (~60-70% original volume) benefits to the increased image volume up to whole mouse by commercialized light sheet microscopy[111]. The cleared samples in organic solutions could be kept for years and reimage by same lab or other labs if needed. However, organic solvents are generally causing irritation to skin, respiratory or eye that should to be handled in ventilation conditions and standard protection of gloves and coats.

Hydrophilic reagent-based clearing technology

The challenges of fluorescent protein emission quench in organic solvents and tissue shrinkage by dehydration inspired the persuasions of hydrophilic reagent-based clearing technology. This type of tissue clearing process uses aqueous chemicals to permeabilize, delipid and match the refractive index. Since water is the basic solvent during the treatment, the hydrogen bonding interactions between water and tissue components are less affected by the dissolving reagents, genetic coded fluorescent proteins could retain the 3D structure then ability of emission after tissue transparency compared to the organic solvent-based methods. Biocompatible hydrophilic reagents widely used include urea, alcohols (e.g. glycerol [116], polyethylene glycol[117,118], sorbitol [119], xylitol, 2,2'-thiodiethanol etc.), sugars (e.g. glucose, sucrose, fructose), DMSO [120] (**Table 1**).

Urea, as the main constitution of Sca*l*e [116], Sca*l*eS [121] and UbasM[122] protocols, is hypothesized to increase internal osmotic pressure of tissue cell membrane, which accelerate the penetration of water and other reagents and result in the decrease of tissue gross refractive index [123]. The hyperhydration of urea induces a slight expansion of tissue, in hence, sorbitol is added in the Sca*l*eS to contract the expansion and keep the original size of tissue. 2,2'-

thiodiethanol (TDE) is firstly applied to clear cultured cell [124], then is shown also workable in clearing of biological tissues [125-129]. Sugar is safe-to-use and easily dissolved in water generating higher refractive index solutions (~1.49). SeeDB[130] and FRUIT[131] use fructose to achieve tissue transparency with original size. These clearing methods are effective for clearing of mouse embryo or brain but inefficient for blood-carrying organs. Hemoglobin is carried by red blood cells which present in all vertebrate species. For rodent models like mouse, the red blood could be removed by perfusion of buffer through the circulatory system (e.g. cardiovascular). However, there is blood clots remained in some organs such as liver, spleen. In the last years, Ueda group developed the CUBIC i.e. “clear, unobstructed brain imaging cocktails and computational anslysis” series protocols [132-136] by extensive screening of chemicals. They identified that aminoalcohols (e.g. N-butyldiethanolamine, 1,3-bis(aminomethyl)cyclohexane, N,N,N’,N’-tetrakis(2-hydroxypropyl)ethylenediamine (Quadrol)) could get rid of the heme inside of remaining blood clot and decolorize the tissue color to improve transparency. Various mouse organs and whole adult mouse are finally cleared enough for imaging. Later, Pende et al. proposed FlyClear[137] to clear *Drosphila* after a special depigmentation using THEED. In CUBIC protocols, new types of refractive index matching solutions were found like sucrose, nitrilotriethanol, antipyrine, nicotinamide to reach ~1.5. Typically, the tissues are passively immersed into clearing mixtures for days to weeks. FOCM [138] was developed as ultrafast optical clearing method and rapidly clarified 300 μm thickness brain slices within 2 minutes. Until now, most of the tissue clearing methods that achieved high tissue transparency by delipidation will not be compatible with lipophilic dyes. For example, DiI could retain in the lipid layers, as a commonly used fluorescent dye for tracing neuronal structures, but cannot apply in tissue clearing. In hence, Zhu et al. developed MACS tissue clearing method by introducing m-xylylenediamine (MADA), which could clear multiple rodent organs or bodies shortly and also be compatible with lipophilic dye probes[119].

Hydrophilic reagent-based clearing technologies are very friendly for transgenic fluorescent proteins and are safe for handling. Several concerns should be kept in mind during the process: 1) The cleared tissues are fragile and slight expanded due to the long incubation time in aqueous solutions, also, are difficult to reimage after several months; 2) Reagents are prepared with high concentration to reach the required refractive index, yet, present high viscosity. 3) Although whole rodent body could be cleared by CUBIC-perfusion or other protocols, no 3D whole body reconstruction is reported but only dissected organs.

Hydrogel-based clearing technology

Hydrogel is a three-dimensional hydrophilic polymer network crosslinking the chains of repeated units in which water is dispersion medium. Introducing hydrogel into the biological tissue to form hydrogel-tissue hybrid for tissue clearing represents a new type of substrate for

chemical and optical interrogation. In this type tissue clearing technology, the biological tissue is: 1) fixed with hydrogel after initiation of crosslinking of monopolymer; 2) delipided by strong detergents such as sodium dodecyl sulphate (SDS) driven by extra force such as electric field; 3) RI matched with aqueous reagent solutions. The covalently linked monomer with tissue elements strength the resistant of tissue to harsh chemical and mechanical treatments by ionic detergents and electrophoresis to get rid of lipids. The resulted hydrogel-embedded tissue with increased hydrophilicity naturally expand the volume following the absorption of water, indicating that the extracellular matrix space of tissue molecules is enlarged for potential macromolecule permeabilization for instance antibody travelling and labeling (**Table 1**).

CLARITY defined as “crosslinked to a three-dimensional network of hydrophilic polymers” is termed by Chung et al. in 2013 to explain the *in situ* hybridization, immunohistochemistry staining of intact nonporous tissue-hydrogel complex system for clearing and imaging[139,140]. In this work, acrylamide and bis-acrylamide are combined with PFA as monomers and VA-044 is chosen as thermal initiator of crosslinking. After the formation of tissue-hydrogel hybrid, electric field is applied across the sample to quickly diffuse highly charged SDS ionic micelles to extract uncrosslinked lipid and other biomolecules. The voltage, temperature and time of the electrophoretic tissue clearing (ETC) are important factors to fast the process while keep tissue intact and fluorescent protein signal[141-144]. Later they introduced SHIELD to stabilize and preserve protein fluorescence, immunereactivity and nuclei acid to harsh conditions of high temperature, alkaline, acid, organic environments using polyfunctional, flexible epoxide[143,145-147]. Based on same ideas, they also created SWITCH to tightly control the antibody binding and stripping interactions inside of tissue to achieve up to 22 rounds of labeling of single tissue by using PH sensitive glutaraldehyde (GA) as crosslinkers[148]. Due to the challenges of implement of ETC system and variability in tissue clarity, Yang et al. proposed PACT (“passive clarity technique”) and PARS (“perfusion-assisted agent release in situ”) to facilitate the hydrogel embedding process by directly delivering optimized monomer solution through systemic circulation and passively remove the lipid using optimized SDS solution, in the end make the tissue transparent in a custom economical recipe of RIMS (refractive index matching solution)[149-153]. Similarly, MiPACT was designed to keep the proteins and RNAs for hybridization chain reaction (HCR) and clear patient sputum to study resided bacterial pathogens[154]. In addition, expansion microscopy (ExM) and expansion pathology (Ex Path) were discovered to perform super-resolution examinations (nanometer scale resolution) of specimen, in which swellable polymers including sodium acrylate or acrylamide were covalently anchored to the tissue[155-159]. The RI matching solutions of tissue-hydrogel hybrids after delipidation could be commercialized FocusClear or glycerol or customized cheaper

RIMS which have refractive index of ~1.46-1.47, while simple deionized water with refractive index of 1.33 could be used in the case of expansion samples.

Hydrogel-based clearing technologies show unique capacity of tissue nuclei acid, RNA, and multiplexed proteome analysis with higher imaging resolution. The infusion of hydrogel provides adjustable parameters to control tissue performances in terms of the degrees of transparency, stiffness, permeability, size or other functionality. However, the challenges of setting up and getting experienced with electrophoresis for efficient clearing of diverse organs limit the wide usability of ECT. Identically, these technologies are still based on aqueous reagents and have the concerns as hydrophilic reagents-based methods as summarized above.

2.4 Current Application of Tissue Clearing

So far, all three types of tissue clearing technologies successfully render main rodent organs, whole rodent and human samples carrying genetic coded or immunostaining fluorescent signals transparent enough for light sheet fluorescent imaging to explore various kinds of biological and biomedical questions. There is no doubt that tissue clearing technologies would significantly and continually contribute to new discoveries in the future following the increasing of adoption to labs across the whole world and commercializing of available approaches[80].

In the terms of rodent (mouse or rat) organs[99,104,105,109,115,133,139,160-164], embryos, brain slice or whole brain, spinal cord, lung tumors, brain tumors, mammary gland, eye, bone, lymph node, lung, kidney, liver, spleen, thymus, thestis, heart, tongue, intestine, pancreas, skull and so on, even whole body of adult mouse were cleared, imaged and evaluated in health and diseased conditions. For example, neuron projection throughout the entire adult mouse central nervous system was firstly reconstructed using uDISCO[111]. ECi focused on the automatically assessment of total numbers of glomeruli as well as the sizes of capillary tuft in murine kidneys[104]. Quantitative changes of bone marrow cells in native environment of intact bone were detected by BoneClarity[160]. Moreover, the possibility of post-immunolabeling with antibodies and dyes provided additional tools to study cell proliferation and brain regional neuronal activity of mouse triggered by drug or exploration task[113,114]. In term of tissue components, the fluorescent signal of cleared tissue could be from protein, RNA, lipid, nuclei acid and exogenous substance (e.g. injected stem cells, cancer cell, adeno-associated virus (AVV) tracers). To better retain the RNA including microRNA inside of tissue, 1-ethyl-3-3-dimethyl-aminopropyl carbodiimide (EDC) is employed to link the 5'-phosphate end of RNA with surrounding amine-containing proteins during the fixation and achieves reliable investigation of activity-associated transcriptional signatures of transparent tissue[165]. AVV

virus injected into mouse brain to label specific neurons are also compatible with organic uDISCO clearing[111] and hydrophilic SHIELD clearing[145]. DiI and DiI-analogues as lipophilic dyes adhering to the lipids of cellular membranes are survived in MACS and CLARITY clearings to mark neuronal axons[119,166]. Besides, tissue clearing technologies are applicable to other species of *dorsophila melanogaster*[99,137], zebrafish[144,167], zebra finch[168], human samples[133,139,145]. Pende et al. combined Flyclear tissue clearing and fused orthogonal images of ultramicroscopy to reconstruct high-resolution 3D details of entire neuronal networks from larval to adult *Drosophila*. CLARITY and PACT could be adopted for imaging intact adult zebrafish to explore the vascular system and immune cell populations [167]. Although some efforts of clearing and imaging human samples showed good results, there still exist many limitations because of the intrinsic nature of human tissue, which will be discussed in the next challenges part.

Overall, depending on the targeted biological questions, any piece of organs from diverse mammal species could be studied by proper tissue clearing method to collect 3D full histological information in single-cell or super resolution across large volume. There are attempts of using tissue clearing to morphological studies of other organisms such as spheroid[169], plant tissue[170,171], insets[172,173] as well as implant-tissue interface[174]. With the single cell spatial and morphological information in 3D, it would be very promising to combine with other technologies to extract cell contents and cell connections, for example, single cell omics (genomics, epigenomis, transcriptomics, proteomics and metabolomics).

2.5 Current Challenge and Prospective of Tissue Clearing

In parallel with the exciting developments and applications of tissue clearing technologies, several challenges are gradually getting exposure regarding to the further optimization of tissue clearing protocols, the quality of imaged fluorescence signal for reliable quantification, the capacity of light sheet microscopy together with the efficiency of data handling and analysis.

With respect to the further directions for expanding tissue clearing technologies, it is obvious that no single methodology could fit all needs. Overview the characters of mice body components as typical animal model, we can generalize the key factors to improve tissue clearing. 1) decolorization of pigments. The colors of body tissue are from different pigments, for instance, red color of blood comes from the heme, the black color of eyeball or fur comes from melanin, the brown color of inner organs comes from the accumulated lipofuscin following aging. These pigments would cause light absorption at visible spectrum (400-600 nm), generate strong autofluoresence across wide spectrum (300-800 nm) and impede the full transparency of tissue. Heme containing blood could be mostly removed from vertebrates by

perfusion of PBS/heparin buffer through the circulatory system. When perfusion is not an option or possible, chemical treatments to destroy the structure of heme and elute the heme from blood clot have to been done, especially in the case of human biopsy. Heme bears a porphyrin tetradentate ligand that binds to an iron ion in the center. Studies show that heme undergoes degradation in the presence of hydrogen peroxide[175], which has already been applied in several tissue clearing protocols[113,114]. Since hydrogen peroxide is a strong oxidant, it potentially adversely affects the fluorescent protein emission and damages tissue microstructures and antigenicity. Another type of chemical candidate is aminoalcohol according to my hypothesis that both of the polarized hydrogen and the electron-rich nitrogen atoms from aminoalcohol would coordinate to the inner iron ion of heme as multidentate ligands to substitute the porphyrin tetradentate ligand, then eluting the red color by destroying the heme complex. Hiroki Ueda's group screened more than 3000 chemicals and found Quadrol, N-butyldiethanolamine, 1,3-bis(aminomethyl)cyclohexane are high efficient and price-costly decolorizations reagents compatible with tissue clearing[133,134]. Melanin is a set of natural pigments and notorious nodus to remove because it is produced through a highly complex biosynthetic process involving oxidation and polymerization of various chemical bonds from heterogeneous monomer units, presenting as opaque, condense and insoluble material. It is reported that extremely reactive species like singlet oxygen, hydroxyl radicals, superoxide anion or hydrated electrons could well react with melanin and probably eliminate them[176-178]. However, these species would be also too harsh to basic protein molecules of biological tissue. Lipofuscin, another type of aging pigment, appears as yellow-brown granules yielded by complicated lipid-content molecules accumulation over longer time of age in common organs of liver, heart, retina, kidney etc. and generates strong autofluorescence, whose mechanisms of formation are still unclear. It will principally affect the clearing and imaging of aged samples like Alzheimer diseased mice or human samples. There are studies to reduce or eliminate lipofuscin autofluorescence using chemicals including Sudan Black B, cooper sulfate, cupric chloride etc.[179-181]. 2) decalcification of bone. Bone structures are dense and rigid mineralized matrix made up of organic components of proteins and inorganic components of mineral salts. The difficulties of sectioning hard bone tissue in histology and clearing call for the necessary of decalcification to get rid of the minerals and make the bone tissue soft enough. Over the years, strong mineral acids (e.g. nitric acid, chloric acid, hydrochloric acid), weak organic acids (e.g. acetic acid, citric acid, formic acid), ion exchange resins, electrolytic devices and chelators (e.g. ethylenediaminetetraacetic acid, EDTA) were tested in decalcification methods[182-184]. Experimental results proved calcium chelating reagents of EDTA-related chemicals are superior to other chelators as a mild and efficient way to soft and loose bone matrix without destroy the tissue, which used in tissue clearing techniques such as Bone Clarity, CUBIC, PEGSOS[115,133,160,185]. In the process of

decalcification by EDTA, PH is an important factor determining the chelating speed adjusted by organic bases or inorganic bases[133]. So far, a combination of chemical cocktails could decolorize all of pigments, decalcification bones of biological tissue and preserve well bioactivity and structural integrity of tissue components is still missing and requires novel inputs and explanations from chemistry understanding (related to **Publication I and II**).

To date, the fluorescent signal of cleared biological tissue could come from transgenic expression of fluorescent proteins for instance GFP, YFP, mCherry etc. or from immunostaining of specific fluorescent dyes or antibodies conjugated with chemical fluorophores. In spite, almost all tissue clearing methods tried to preserve the fluorescent protein emission as long as possible, as bright as possible, its signal-to-background ratio is relatively lower in visible spectrum, where skeletal muscles and bones possess obstructive autofluoresce. For example, Kubota et al. developed CUBIC-cancer tissue clearing method to render the transparency of whole body of mice, but had to image dissected specific organs from transparent whole mice to check single cells information because the fluorescent protein signal of labeled cells distributed inside of whole body is not bright enough to be captured through the thick muscles and bones[135]. By comparison, chemical fluorophores are designed to tune the spectral and quantum yield properties using chemistry to increase the brightness and photostability in various environments[186]. The antibody conjugated fluorophores include Alexa or Atto families across 390-740 nm, whose optical properties are nearly independent of solvent and temperature. For small molecular dyes, rhodamine, propidium iodide (PI) and TO-PRO-3 are successfully incorporated into whole mice labeling and clearing to indicate cell nucleus in CUBIC or uDISCO protocols. However, it is significantly challenging to specifically label cellular structures using antibody. Antibodies are large-size (~150kD), Y-shaped proteins recognizing unique antigens, which could not penetrate deeply into the tissue, with a limitation of several hundred micrometers. To improve the antibody labeling capacity, iDISCO protocols used chemicals of methanol, DCM and H_2O_2 to pretreat the tissues, which allowed antibody binding and quantification of signal across whole mouse brain at the expense of sacrificing some antigen activity[113,114]. CLARITY transported antibodies deep inside of tissue by electrophoresis following a throughout delipidation using SDS[142]. These reported progresses yet restricted to mouse inner organs, then an efficient and reliable whole-body immunolabeling and clearing method would substantially benefit to panoptic and quantitative studies of organism in both of health and disease conditions, in particular, most disease although initiating in a local spot finally affect all parts of organism over time (related to **Publication II**).

Since the regular and powerful *in vivo* labeling technologies including transgenic proteins or unapproved fluorescent dye injection cannot apply to human body, the investigations of post-

mortem human organs focusing on cellular and molecular cross-examinations have to rely on post-staining methods using all kinds of dyes and antibodies. As we all known, antibodies generally have large molecular weights (~150 kDa) and cannot penetrate deeply inside of condense tissue. In standard histology, decades-aged human samples need to be cut into 50-100 µm thick sections for antibody permeabilization. The cutting-edge techniques reported by prior tissue labeling and clearing methods could achieve maximum of ~1 mm thickness human slice antibody labeling. uDISCO, CLARITY, SWITCH or CUBIC allowed successful small molecule dye labeling and clearing of < 2-mm-thick human clinical sample[111,133,139,148]. Liu et al. reported that human brain cortical tissue required around 3~4 times longer processing than rodent tissue using passive CLARITY, similarly, it took at least 10 month to label and clear 3-mm-thick human brain cortex using active CLARIRY method[187,188]. OPTIClear was proposed to clear human brain tissue but a piece of human striatum tissue of 5 mm thickness needed about 3.5 months to render transparent[189]. MASH was described as a simple, fast and cost-effective optical labeling and clearing approach for human cortex samples adapted from iDISCO+, by which 5 mm thick samples could be stained and cleared in 10 days[190]. It is obvious that the labeling and clearing of human samples are more difficult than rodent organs. It is summarized as three reasons. 1) Lipofuscin is a post-mitotic pigment composed of a admixture macromolecules through oxidization and cross-linking of diverse proteins, lipids and sugars produced during metabolic processes[191]. It will accumulate daily and prominently appear when people are aged in most human organs, especially in the brain, relating with senescence and sturdiness[191]. 2) Similarly, nonenzymatic glycosylation and insoluble collagen will become more and more with aging, resulting in the hardening and browning of collagen and causing autofluorescence[192]. 3) The complexity of lipidome in human organs compared to chimpanzee, monkey or mouse makes human tissue difficult to inquire. Because of the gradual accumulation of all such changes in human body across whole life, the histological study of post-mortem organs showed much more challenges when using big molecular dyes or antibodies, even though adopting advanced tissue labeling and clearing methods that are already successful on rodent sample. The rodents would be generally sacrificed after several months of born, avoiding many age-related problems. The labeling and clearing of human organs requires a systematic understanding of tissue components and a different interrogation way. (related to **Publication I**).

Light-sheet fluorescent microscopy, as an insufficient four-dimensional (4D; x, y, z and t) imaging strategy of combining optical sectioning and parallelization, permits long-term sample recording with less phototoxicity but rapid acquisition[193]. The broad adoptions of tissue clearing technologies to various organisms ask for high capacity of imaging systems[194,195]. Lavision BioTec Ultramicroscope and Zeiss Lightsheet Z.1 are the most used commercialized systems,

facing several challenges. 1) High-resolution over a large field of view (FOV). Numerical aperture (NA) of LSFM determines the light-sheet length and thickness. High NA detection optics performs well in collecting light and generates fine lateral resolution, on the other side, high NA illumination creates a thinner plane of light, leading to small achievable FOV. Basically, it is a trade-off to balance incompatible features of usable FOV and axial resolutions. For instance, 0.06>NA>0.02 will give a cover of FOV around 50-500 μm[196]. The NA of sheet optics in Lavision BioTec Ultramicroscope II is 0.0148-0.148. 2) The accommodation chamber capacity. Another obstacle of imaging cleared rodent whole bodies is the big size of sample cannot fit into a proper sample holder and imaging chamber. The dimensions of transparent mice with a volume shrinkage of 30% from uDISCO is around 10 cm x 6 cm x 3.5 cm and Lavision BioTec Ultramicroscope II has an imaging chamber of 8 cm x 8 cm x 3.5 cm (with travel range of 1 cm x 1 cm x 1 cm). Samples had to be mounted by costumed holders and imaged piece by piece with cutting[111], which took extra time and efforts to stitching and fused all pieces into whole mice. 3) The working distance (WD) of objectives. When measuring over large volume using subaperture stitching, it is important to control the z defocusing and to inspect deeply with suitable lateral resolution. The WD of Most of the high magnification objectives cannot cover the whole thickness of adult mouse. For example, the 2x objective lens of Lavision BioTec Ultramicroscope II has a WD of 6 mm, 1.1x NA 0.1 MI PLAN objectives with dipping caps have WD of 5.6-17 mm. Advanced custom-designed objectives are very expensive, complex and prohibitive for the majority of microscopists[197]. Other improvements related to attenuate artifacts of LSFM[198], ease-of-use and throughput with open-top light-sheet (OTLS)[199], non-invasive LSFM in near-infrared II[200], two-photo light sheet microscopy with accelerating beams[201], adaptive light-sheet microcopy for living organisms[202,203], low-cost cleared tissue digital scanned light-sheet microscopy (C-DSLM)[204] have been conducted to optimize the imaging systems for diverse applications. Recently reported mesoSPIM set out to achieve large imaging volume (travel range across 44 mm × 44 mm × 100 mm) and outstanding image quality across a large FOV (axial resolution of 6.52±0.07 μm across FOV of 13.29 μm) with simple and versatile sample handling (CLARITY, CUBIC, DISCO), representing a promising open-source platform in future[205]. We can see LSFM will continuously be developed and implement innovations in the light of growing needs for simple, fast, high quality and big volume imaging of whole organisms even with intact human organs (related to **Publication II**).

In parallel with the high resolution and big volume imaging of whole organisms with LSFM, a remarkable set of raw data (e.g. a single whole mouse produces 2-3 terabytes) is generated and calls for powerful computers with hardware to store, handle and analyze the information. *Image J* or *Fiji*, as an open-source java-based image processing program, is developing to

serve users via functional plugins including stitching, segmentation, visualization or color profiling data[206,207]. *Imaris* is a commercialized product from Bitplane to provide functionalities of visualization, segmentation and interpretation of 3D and 4D microscopy data. Beside, specific software, *ClearMap*, was developed to analyze 3D datasets obtained from iDISCO+ for object detection, registration and statistics[114]. Zeng group reported NeuroGlobalPostion-Systerm (*NeuroGPS*) to achieve automatically tracing individual neurons across large neuronal populations based on the strategies of mimicking human processing[208]. These platforms are user-friendly, ready-to-use but have limitations to handle big raw data in terms of speed, accuracy and adjustable parameters for analyzation, because they mainly depend on filter-based adjustments (e.g. thresholding or watershed algorithms) that are impossible to apply to scaled data of terabytes with high heterogeneity. In contrast, deep learning architectures have the ability to generalize in non-local and global ways, in which possible configurations of features or weights are feasible to give a compact configuration from each data then result in a richer generalization[65,209]. For example, Todorov et al. developed vessel segmentation and analysis pipeline (VesSAP) to systematically analyze vascular features of cleared mouse brain including the length, bifurcation points and radius by registering into Allen brain atlas using fully convolutional network[70]. Now, big data are quickly expanding in all science domains, following a substantial computation requirement. It have been reported that well-approving accuracy needs to train the large neural networks on 100s or 1000s of severs for days[210]. Laboratory workstation with Graphical Processing Unit (GPU) attached to a single machine is also known to work for scalable neural network trainings[70,71,211]. In DeepMACT, one round of training over 40 epochs was finished in about 20-30 minutes using a commercialized workstation attached with a NVIDIA Titan XP GPU[71]. In future, limited shared memory and inter-machine communication still exists a challenging job, cloud computing has been seen as rising options[212,213] (related to **Publication II**).

3. Research Aims

There has been a long-term debate regarding to the potential of both value and methodology to fully elucidate the structures and cells of a whole organism. Scientists have developed multiple approaches using different spatial scales to achieve this. My project aimed at the holistic 3D cellular mapping of mammalian organs applying tissue clearing technologies. I wanted to pursue the following aims:

1) To develop a scalable and robust tissue labeling and clearing technology for centimeter-sized and decade-aged human organs to investigate cellular and molecular information. Specifically, I wanted to understand human organs towards a comprehensive view of their complex chemical components and to identify the key factors that affect the distribution of clearing and labeling reagents into and within whole

organs. By searching and screening large numbers of chemicals that interact with tissue-compositions, I wanted to develop a new tissue clearing and labeling protocol using chemical cocktails. This protocol would allow small molecular dyes and antibodies to freely penetrate into centimeter-sized human tissue for effective labeling and achieve whole human organ transparency, while matching the refractive index. My aim was, capitalizing on a powerful light sheet fluorescent microscopy, to record a full map of inner structural and cellular signals from labeling and to 3D reconstruct images from the transparent human organ. To analyze the big data sets of 3D whole organ images in a fast and accurate way, deep learning algorithms were to be employed. In sum, my project aimed at combining multidisciplinary knowledge of chemistry, engineering, biology, computer to provide a non-sectioning way for 3D mapping of intact human organs at single cell resolution. At the same time, this approach was meant to be simple, cost-effective, labor-efficient and easily adoptable.

2) To develop a whole-body immunolabeling method to enhance fluorescent signals allowing reliable quantitative studies in health and disease. The method was going to be based on nanobodies, which are about 10 times smaller than antibodies, and can thus travel deeper inside the tissue. I wanted to establish chemical fluorophores conjugated to nanobodies that could sustain an enlarged signal intensity compared to the transgenic endogenous fluorescent protein in a given mouse model. By introducing a pump system, the fluorescent nanobody would be delivered into body of the mouse to achieve efficient immunolabeling. The aim was to optimize this technology in a way that it would be compatible with tissue clearing and offer a strong nanobody signal that could be scanned and analyzed through all layers of body including skin, muscle, bone and so on. With this technology, any body part of a mouse could be investigated in a panoptic view to understand the cellular and structural information in both physiological and pathological conditions. Another goal was to applied this to disease mouse model such as neurodegenerative disease, cancer metastasis, and study nanomaterial efficacy.

4. Research Summary

In this work, I systematically investigated the tissue component complexity of decade-aged human organs and accordingly developed tissue labeling and clearing protocols using chemical cocktails to allow antibodies, dyes and other reagents travelling through the intact human organs to achieve homogenous labeling and transparency. Firstly, I identified CHAPS as a key permeabilization detergent to interact with sturdy and condense human tissue and make it accessible. Based on the detergent, I developed SHANEL (small small-micelle-mediated human organ efficient clearing and labeling) to clear and label intact adult human

organs (e.g. kidney, brain and thyroid) to be transparent enough for imaging. In the end, I reconstructed the 3D maps of transgenic pig pancreas, intact human eye, human thyroid and human kidney carrying structural and molecular details after light-sheet fluorescent imaging. Furthermore, I helped to analyze the numbers of millions cells in human brain cortex and hippocampus by a deep learning pipeline. In conclusion, SHANEL was developed as a reliable, scalable and unbiased way to generate the full charts of large intact mammalian organs with cellular and molecular architectures.

To achieve a panoptic evaluation of the whole rodent body in a quantitative and robust way, I helped to developed the vDISCO (nanobody(V_HH)-boosted 3D imaging of solvent cleared organs) technology to systematically study the biological functions in both health and disease. This technology is based on a pressure-driven pump to deliver stable and small-sized nanobodies across a whole mouse through the circulation. I participated in optimizing the protocol involving various types of chemicals for labeling and clearing. In the end, we generated a cleared “invisible” adult mouse that showed strong fluorescent signals inside. Due to the high quality of the fluorescent signals (up to ~100 of magnitude), several diseases (e.g. stroke, traumatic brain injury) morphological features and fragile structures were identified. For example, I revealed the small connections between brain meninges and skull bone marrow by imaging the whole mouse brain through skull after labeling and clearing. And there were immigrating immune cells in the case of stroke. Hence, vDISCO technology allows a more comprehensive study of local disease and their effects on the rest of body in an unbiased way.

PUBLICATION I

DOI https://doi.org/10.1016/j.cell.2020.01.030

Cellular and Molecular Probing of Intact Human Organs

Shan Zhao, Mihail Ivilinov Todorov, Ruiyao Cai, Rami AI-Maskari, Hanno Steinke, Elisabeth Kemter, Hongcheng Mai, Zhouyi Rong, Martin Warmer, Karen Stanic Aguilera, Oliver Schoppe, Johannes Christian Paetzold, Benno Gesierich, Milagros N. Wong, Tobias B. Huber, Marco Duering, Oliver Thomas Bruns, Bjoern Menze, Jan Lipfert, Victor G. Puelles Rodriguez, Eckhard Wolf, Ingo Bechmann, Ali Ertürk

Contribution to the publication

As the first author of this publication, I was deeply involved in the conception of the study, performed most of the experimental work and wrote the manuscript together with the corresponding author Ali Ertürk. I developed SHANEL protocols to achieve labeling and clearing of thick mammalian organs. Firstly, I identified CHAPS as an efficient permeabilization small-micelle-detergent and screened compatible chemicals for blood decolorization (Fig 1 D-I, Fig S1 D-I). Secondly, using SHANEL clearing protocol, I made the whole pig brain and whole human brain transparent and reconstruct the islets distribution of *INS*-EGFP transgenic pig pancreas and human eye (Fig 2 A-L, Fig 3 A-E). Thirdly, I further developed SHANEL histology protocol to allow antibody-sized molecules to travel into centimeter-thick sturdy human brains (Fig 4 A-N, Fig S4 A-H, Fig S5 A-F). Then, intact human kidney and thyroid were cleared, imaged and analyzed using a new prototype light-sheet microscope (Fig 5 A-G, Fig 6 A-K, Fig S7 A-D). To efficiently handle big data, deep-learning-based quantification method was developed based on ground truth data and unseen data of 3D cell reconstruction of human brain samples (Figure 7 D-E). Comparison with other tissue clearing methods, SHANEL is unique, robust and powerful to label and clear mammalian tissues without destroy the microstructures (Fig S2 A-C, Fig S7 E-H).

PUBLICATION II

DOI https://doi.org/10.1038/s41593-018-0301-3

Panoptic imaging of transparent mice reveals whole-body neuronal projections and skull–meninges connections

Ruiyao Cai, Chenchen Pan, Alireza Ghasemigharagoz, Mihail Ivilinov Todorov, Benjamin Förstera, Shan Zhao, Harsharan S. Bhatia, Arnaldo Parra-Damas, Leander Mrowka, Delphine Theodorou, Markus Rempfler, Anna L. R. Xavier, Benjamin T. Kress, Corinne Benakis, Hanno Steinke, Sabine Liebscher, Ingo Bechmann, Arthur Liesz, Bjoern Menze, Martin Kerschensteiner, Maiken Nedergaard, Ali Ertürk

Contribution to the publication

As a co-author of this publication, I made contributions to partial experimental work and I revised the manuscript. During the development of vDISCO protocol, I screened chemicals for decalcification of mice bones and identified the concentration of EDTA, which was incorporated into the whole body immunelabeling and clearing protocol. In addition, I disclosed the short skull-meninges connections at the brain and sagittal sinus interfaces (Figure S20 a-b and video S9).

ADDITIONAL CONTRIBUTIONS

Single cell precision use of DNA nanotechnology in whole body

Summary

The drug delivery and gene editing technologies require cell level precision to be most effective in treating diseases. DNA nanotechnology can overcome these challenges as the Origami structures are biocompatible and programmable for multiple functions. However, application of nanotechnology at single cell precision has remained a challenge. To enable cell-level use of DNA nanotechnology in vivo, we first generated immune tolerable DNA Origami at therapeutic amounts, then, track their biodistributions at cell level in transparent mice after vDISCO whole mouse clearing. We showed CX3CR1 antibody-conjugated Origami targeting of individual immune cells throughout the mouse body. Furthermore, we loaded an antibody-based cancer drug on Origami and targeted individual cancer cells for the first-time using DNA nanotechnology. Thus, our approach can significantly help developing DNA nanotechnology for *in vivo* applications including drug delivery and gene editing.

Introduction

Historically, drug development is defined as a long-term, high-risk and costly endeavor[214]. While bioactive drug candidates for incurable diseases (e.g. cancer, neurodegenerative disease, genetic disease etc.) like antibodies or gene/cell-based therapies have been promoted from bench towards clinical trials soon, open debates related to feasible administration routes, long-term potential safety, therapeutic mechanisms and efficacy *in vivo* are still existing[215]. It is highly required unequivocal strategies to achieve both targeting and monitoring precisely at single cell level in whole body of mice to facilitate drug development process. Combination of molecular targeted-therapy and molecular imaging for *in vivo* administration would hold great promise to provide sufficient information in a practical way[215,216]. Considering the complex system involving different types, numbers and sizes of diverse molecules as therapeutic drug, guided triggers and imaging agents, we set our goals based on DNA origami, which is biocompatible, nanometer-size and programmable platform[217] allowing flexible introducing of chemical functionalities to regulate the dose, timing, and location of drugs.

DNA origami, as one unique type of designable delicate three-dimensional structure of nanomaterial[218,219], is characterized by the outstanding capability of hybrid with diverse inorganic (e.g. silver[220], gold[220-222], ruthenium[223] etc.) and organic (e.g. protein[224,225], oligonucleotides[226,227], peptide[228], dye[229], lipid[230], polymer[231] etc.) molecules for transformative applications including biosensor[226,232], materials science[220], disease theranostics[221], photonic

device[227,229] and drug delivery[223,228,233]. Comparing to the success of creative studies using DNA origami in vitro, its practical applications by *in vivo* administration are suffering challenging hurdles[218]. First, economic mass production of scaffold and staple DNA up to milligram is needed to support repeated animal experiments, since commercially available staple strands of origami structure by synthesis ways cost thousands of dollars[234]. Second, the introduction of exogenous DNA will cause potential biosafety problems by eliciting influential immune responses. Third, although cell-based assays demonstrated DNA origami structures were stable enough to enter cells by endocytosis[235], the understanding of pharmacodynamics stability in real physiological condition of changeable environment are poor. In the end, as a leading example, how the spatial addressability and efficacy of drug delivery in mice by DNA origami with increased drug cargo capacity?

To address these questions and explore the strategy of using DNA origami as substrate for molecular therapy and molecular imaging in whole mouse, we employed tissue clearing and imaging technology as readout evaluation method. Recently, improvements in advanced equipment and elegant iterative image analysis of multimodality imaging, for example, PET/SPECT, PET/MRI, PET/CT, provide synergistic anatomical information of drugs, they still are subject to low resolution, which lack cellular and molecular parameters[236-238]. Tissue clearing and imaging technology as an emerging tool already achieved whole mouse transparency[239] and 3D reconstruction at single cell resolution, which were successfully used to study neuronal connectivity in physiological and pathological conditions[240], in addition to quantitatively detect single cancer metastasis and drug targeting in several cancer models[241].

Here, we showed a mass-productive DNA origami are safe, stable for *in vivo* studies as powerful vehicle to deliver and monitor drugs in single cell precision by tissue clearing and imaging technology, which represented a promising strategy to perform accurate preclinical evaluations of new therapeutic drugs including antibody and gene editing to accelerate drug development.

Results

Immunogenicity Assessments

Since the single-stranded DNA is actual mass-produced inside *Escherichia coli* with a stirred-tank bioreactor[234], it is highly possible that residual endotoxin after removing bacterial fragments would cause *in vivo* immune reactions. Endotoxin[242], also referred lipopolysaccharide, could be found in all essentially Gram-negative bacteria including *Escherichia coli* as the main composition of its outer membrane and is well-known to induce inflammation. Furthermore, to enhance the stability of DNA origami in physiological dynamic

environments that are full of diverse enzymes, they were coated with poly(ethylene glycol)-poly(L-lysine) (PP) cationic polymer, whose lysine residues could entangle with the phosphate residues of DNA through positive-negative electrostatic interactions and protect against nuclease digestion[243]. In order to evaluate the *in vivo* immune responses of mass-produced DNA nanorod origami, we injected 100 µL of $MgCl_2$ folding buffer ($MgCl_2$ buffer), 100 µL of 2µM original DNA nanorod without further purification (unPuri), 100 µL of 2µM DNA nanorod with purification to remove endotoxin (Puri) and 100 µL of 2µM purified DNA nanorod coating with poly(ethylene glycol)-poly(L-lysine) (Puri-PP) to mixed gender CD-1 mice through the tail vein, respectively. After 4 hours or 24 hours circulation, the mice were scarified to collect blood and spleen for immunophenotypic analysis with flow cytometry (**Figure 3A**). Indeed, the original mass-

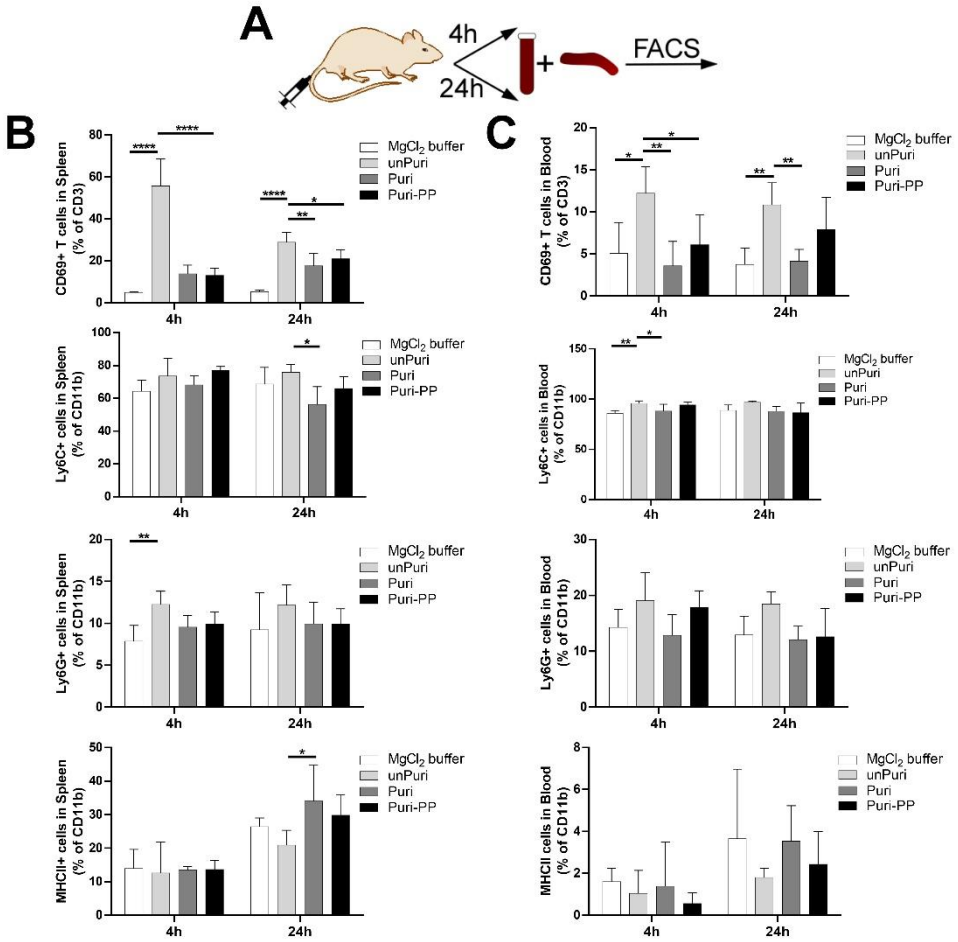

Figure 3 Immunogenicity assessments of DNA nanorod origami in CD-1 mice after tail vein injection. **(A)** Schematic illustration of animal experimental process: the blood and spleen were collected for flow cytometric analysis after 4 h or 24 h tail vein injection of DNA nanorod (100 µL, 2 µM). FACS quantifications of CD69+CD3+ T cells, Ly6C+CD11b+ monocytes, Ly6G+CD11b+ monocytes and MHCII+CD11b monocytes in spleen **(B)** and blood **(C)** indicated decreased immune responses in CD-1 mice after 4h or 24h administration of purified DNA nanorod comparing to the group of unpurified with residual endotoxin, similar to poly(ethylene glycol)-poly(L-lysine) coated purified DNA nanorod. (n=5, p values were calculated with one-way ANOVA multiple comparisons)

produced DNA nanorod elicited strong immune reactions with increased CD69+CD3+ T cells in blood and spleen, both shown acute immune response after 4 hours and adaptive immune

response after 24 hours. After further endotoxin purification, the immunogenicity of DNA nanorod greatly decreased, which was similar to that of the PP coated DNA nanorod (**Figure 3B-C**).

Next, we want to check the in vivo immunogenic safety of large amount of DNA nanorod administration by gavage (**Figure 4A**). 400 µL of 2µM purified DNA nanrod or PP coated purified DNA nanrod was delivered through gavage to mixed gender CD-1 mice. The mice were scarified to collect blood, spleen and payer's patches for flow cytometry analysis at 24 hours and 7 days. For the 7 days group, physiological assessments were performed including

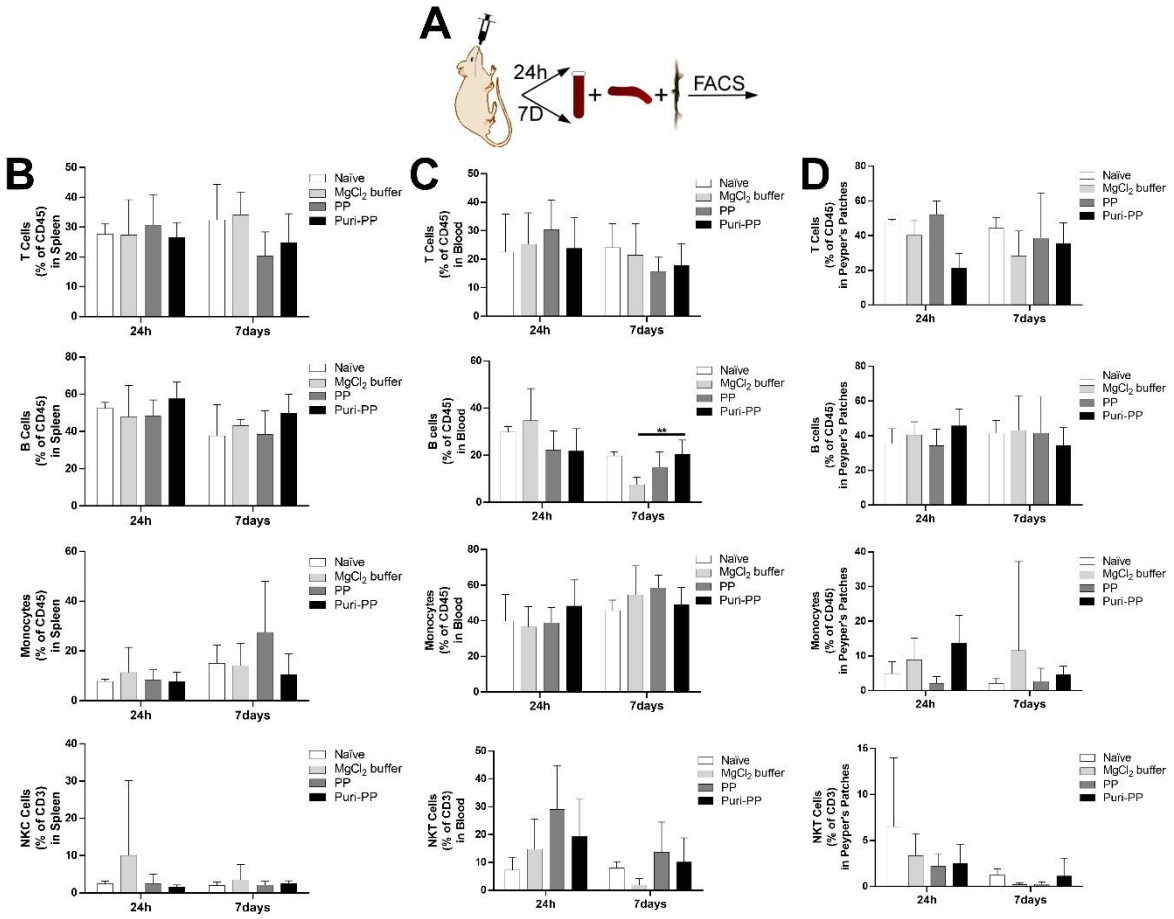

Figure 4 Immunogenicity assessments of DNA nanorod origami in CD-1 mice after gavage.
(A) Schematic illustration of animal experimental process: the blood, spleen and payer's patches were collected for flow cytometric analysis after 24 h or 7 days gavage administration of DNA nanorod (400 µL, 2 µM). FACS quantifications of CD45+ T cells, CD45+ B cells, CD45+ monocytes and CD3+ natural killer T cells in spleen **(B)**, blood **(C)** and payer's patches **(D)** indicated no immune responses in CD-1 mice after 24h or 7days administration of poly(ethylene glycol)-poly(L-lysine) coated purified DNA nanorod comparing to the control groups. (n=6, p values were calculated with one-way ANOVA multiple comparisons)

body weight, body temperature and basic neurological tests of motor and behavioral deficits on day 0, day 1, day 3, day 5 and day 7. By checking the numbers of CD45+ T cells, CD45+ B cells, CD45+ monocytes and CD3+ natural killer T cells in blood, spleen and payer's patches, we did not observe immune responses from DNA nanorod groups comparing with the naïve

and buffer controls (**Figure 4B-D**). Also, DNA nanorod did not cause physiological changes (**Figure 5A-C**).

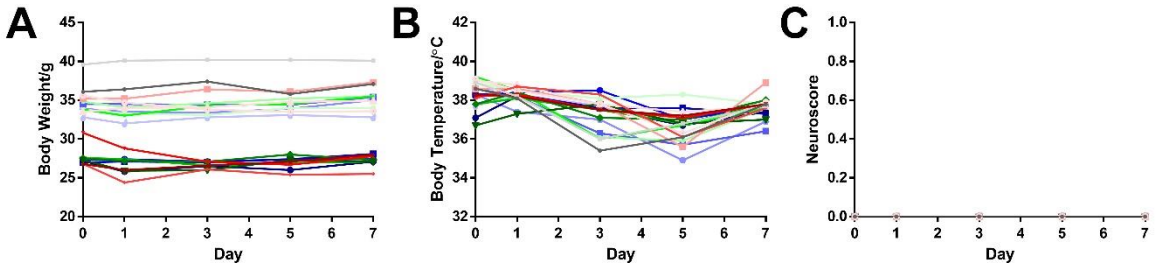

Figure 5 Physiological assessments of CD-1 mice after DNA nanorod origami gavage.
The physiological follow-ups of CD-1 mice at day 0, 1, 3, 5, 7 after DNA nanorod gavage in terms of body weight **(A)**, body temperature **(B)** and neuroscore **(C)** for basic sensory and motor examination.

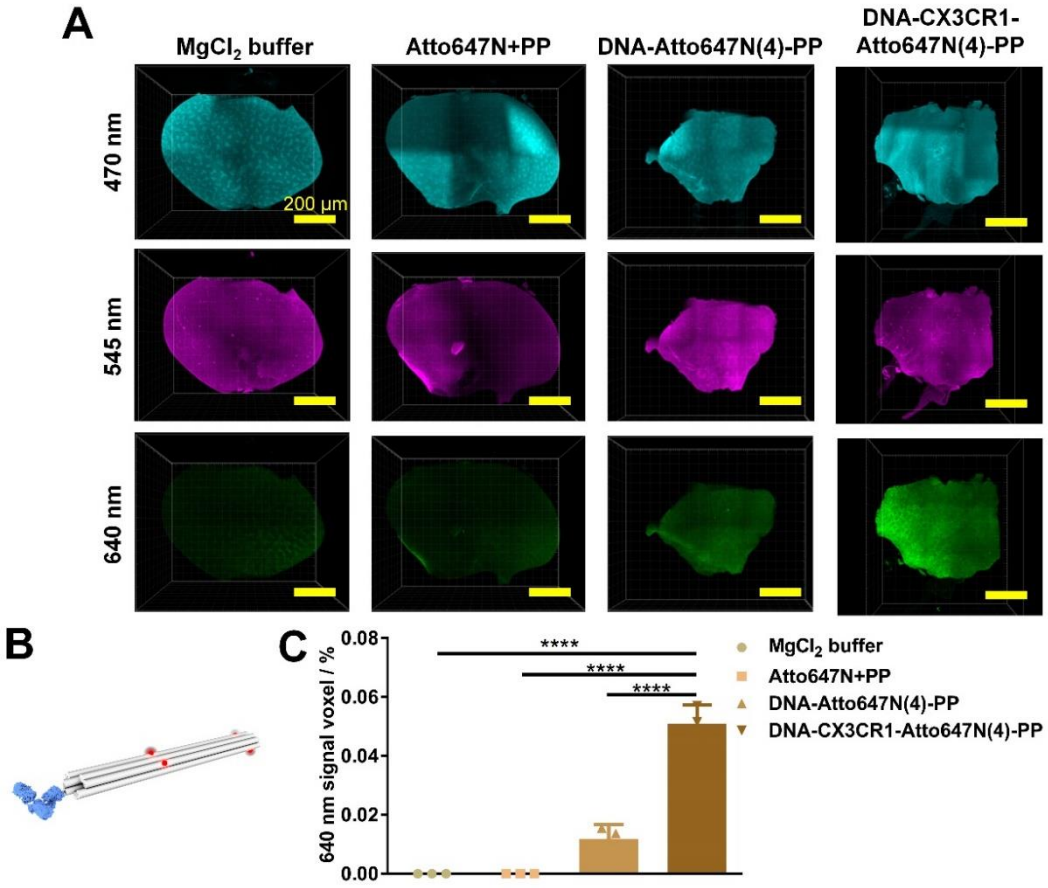

Figure 6 3D reconstruction of cleared liver from CX3CR1-GFP mice after DNA origami administration.
(A) 3D reconstruction of light sheet fluorescent microscope images of cleared liver organs from CX3CR1-GFP mice after 20 min administration of DNA origami (100 μL, 1 μM). The first panel showed background signal of liver at 470 nm wavelength since CX3CR1-GFP signal was killed by vDISCO tissue clearing method. The middle panel showed propidium iodide labeled cell nuclei at 545 nm wavelength. The third panel showed DNA nanorod origami signal at 647 nm wavelength. The DNA-CX3CR1-Atto647N(4)-PP group had significant higher origami signal compared to the DNA-Atto647N(4)-PP group without CX3CR1 antibody. There was no signal in mice of injecting mixture of Atto647N dye and poly(ethylene glycol)-poly(L-lysine). **(B)** The design of DNA-CX3CR1-Atto647N(4)-PP nanorod origami containing 1 CX3CR1 antibody and 4 Atto647N dyes. **(C)** Quantification of voxel percentage of 640 nm wavelength signal from DNA origami in liver. (n=3, p values were calculated with one-way ANOVA multiple comparisons)

In vivo targeting, clearance and biodistribution at cellular level using tissue clearing technology

To monitor the *in vivo* behaviors of DNA nanorod at cellular level, we conjugated 4 Atto647N dyes on the DNA nanorod followed with PP coating (DNA-Atto647N(4)-PP), in addition to 1 CX3CR1 antibody linked at one end of DNA-Atto647N(4)-PP (DNA-CX3CR1-Atto647N(4)-PP).100 µL of $MgCl_2$ folding buffer ($MgCl_2$ buffer), 100 µL of mixture of 4µM Atto647N dye and PP solution (Atto647N+PP), 100 µL of 1µM DNA-Atto647N(4)-PP and 100 µL of 1µM DNA-CX3CR1-Atto647N(4)-PP were injected into CX3CR1-GFP mice by femoral vein. To check the targeting effects, the mice were scarified after 20 minutes following with vDISCO tissue clearing process and light sheet fluorescent microscope imaging[240]. By checking the liver organs where host a lot of immune cells, we found DNA-CX3CR1-Atto647N(4)-PP group mice had significant higher targeting effects compared to the DNA-Atto647N(4)-PP group without CX3CR1 antibody from the quantitative voxel percentage of 640 nm signal (**Figure 6A-C**).

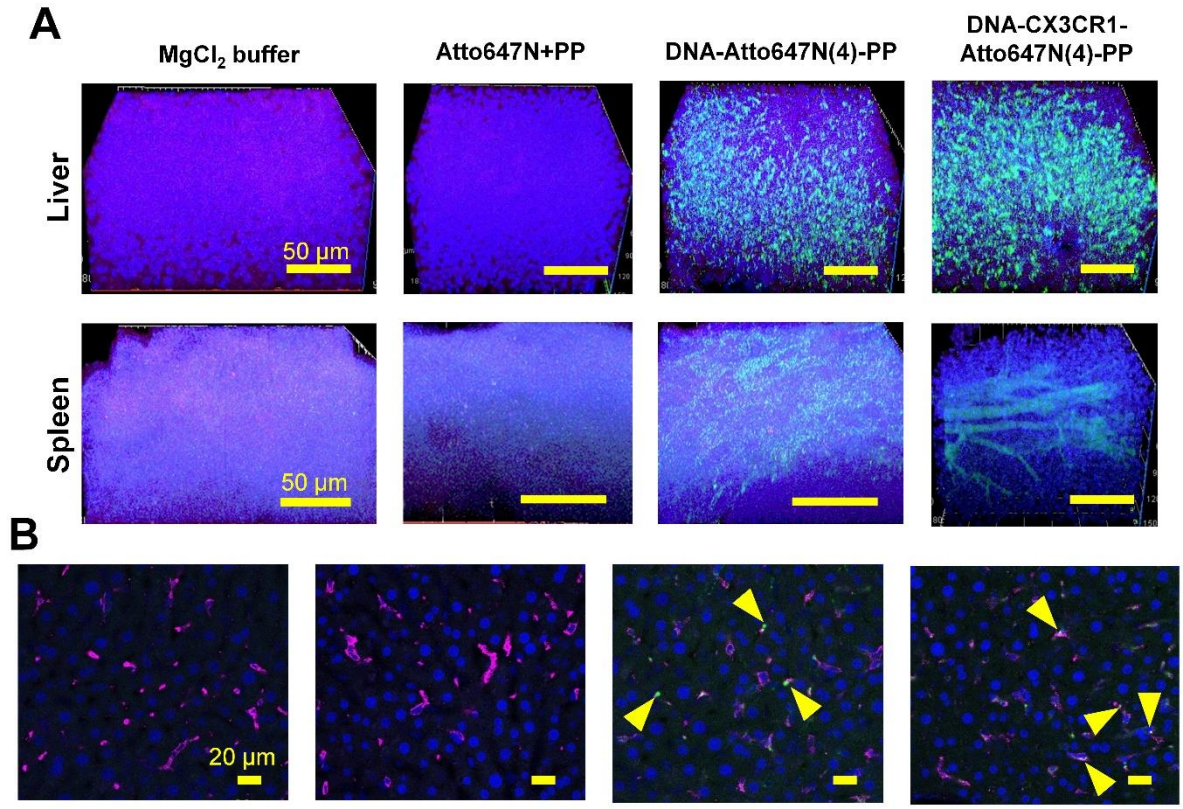

Figure 7 Confocal microscope examinations of cleared liver and spleen from CX3CR1-GFP mice after DNA origami administration.
(A) 3D reconstruction of confocal fluorescent microscope images of cleared liver and spleen organs from CX3CR1-GFP mice after 20 min administration of DNA origami (100 µL, 1 µM). Blue represents propidium iodide labeled cell nuclei and green represents DNA nanorod origami signal. The DNA-CX3CR1-Atto647N(4)-PP group had significant higher origami signal compared to the DNA-Atto647N(4)-PP group without CX3CR1 antibody. There was no signal in mice of injecting mixture of Atto647N dye and poly(ethylene glycol)-poly(L-lysine). **(B)** Confocal images of liver slice (1mm thick) stained with Iba1 antibody indicating microphages. Blue: propidium iodide labeled cell nuclei; Magenta: Iba1 labeled microphages; Green: DNA origami, highlighted with arrow.

This means CX3CR1 antibody guides the DNA origami to the cells and increases the uptake of DNA origami in the cells. The same results were also proved by magnification images of both liver and spleen using confocal microscope (**Figure 7A**). Next, immunostaining of ionized calcium binding adaptor molecule 1 (Iba1) antibody with rehydrated liver slice shown that DNA

nanorod were swallowed by monocytes and macrophages (**Figure 7B**). We also noticed that there was no signal in organs of injecting mixture of Atto647N dye and PP (**Figure 6A, 7A-B**), which well demonstrated that the DNA nanorod were taken inside of the cells not the Atto647N dye degraded from the origami.

To check the clearance effects, the mice were scarified after 20 minutes, 4 hours and 24 hours, which were cleared with vDISCO tissue clearing method. From the light sheet fluorescent microscope images of liver organs, the DNA-Atto647N(4)-PP origami signal was significantly reduced after 4 hours and disappeared after 24 hours (**Figure 8**). This is in line with the requirements of good nanomaterial that not only reaches to the targeted cells but also cause no accumulation in body.

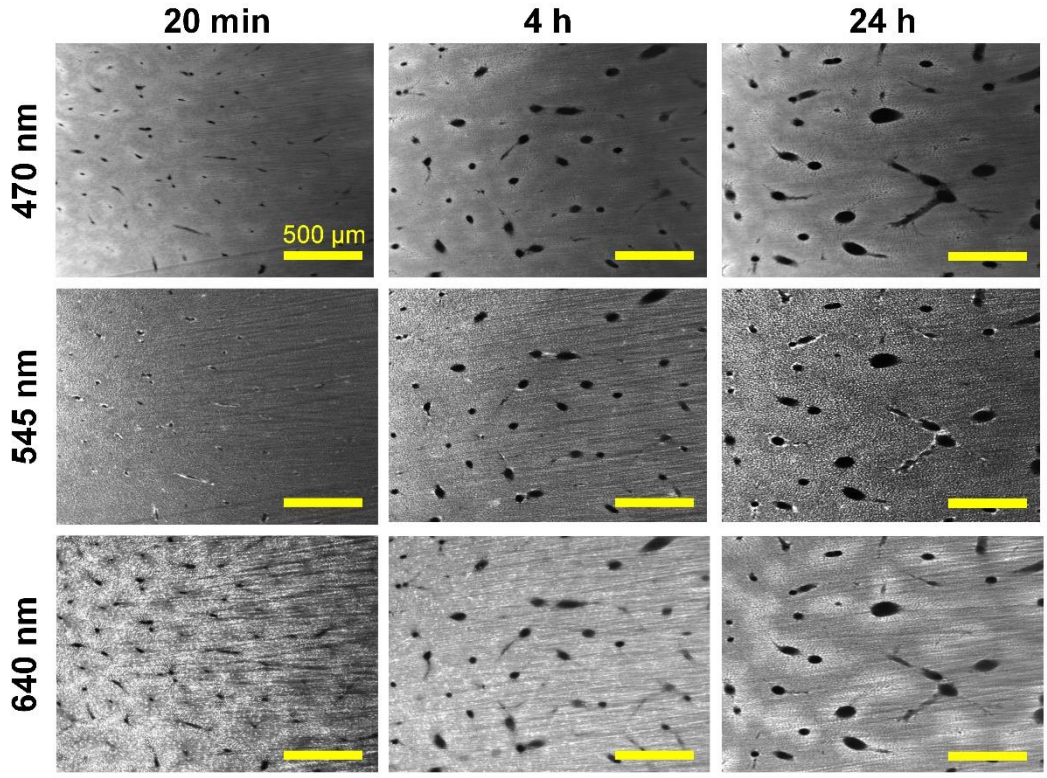

Figure 8 *In vivo* clearance of DNA-Atto647N(4)-PP nanorod origami in CX3CR1-GFP mice after femoral vein administration.
Light sheet fluorescent microscope images of transparent liver organs from CX3CR1-GFP mice after 20 min, 4 h and 24 h administration of DNA-Atto647N(4)-PP nanorod (100 µL, 1 µM). The first panel showed background signal of liver at 470 nm wavelength since CX3CR1-GFP signal was killed by vDISCO tissue clearing method. The middle panel showed propidium iodide labeled cell nuclei at 545 nm wavelength. The third panel showed DNA nanorod origami signal at 647 nm wavelength, which reduced after 4 h and disappeared after 24 h.

To have an overview of DNA nanorod biodistribution in whole body of mice, CX3CR1-GFP mice injected with DNA-CX3CR1-Atto647N(4)-PP was 3D reconstructed. Muscles were observed with strong autofluorescence at 470 nm wavelength, wherein, internal organs and bone marrow were shown with propidium iodide (PI) labelled amounts of cell nuclei. We found

that CX3CR1 guided DNA nanorod were accumulated in liver, spleen, lymph node and stool according to the signal from 640 nm wavelength, where host immune cells (**Figure 8**).

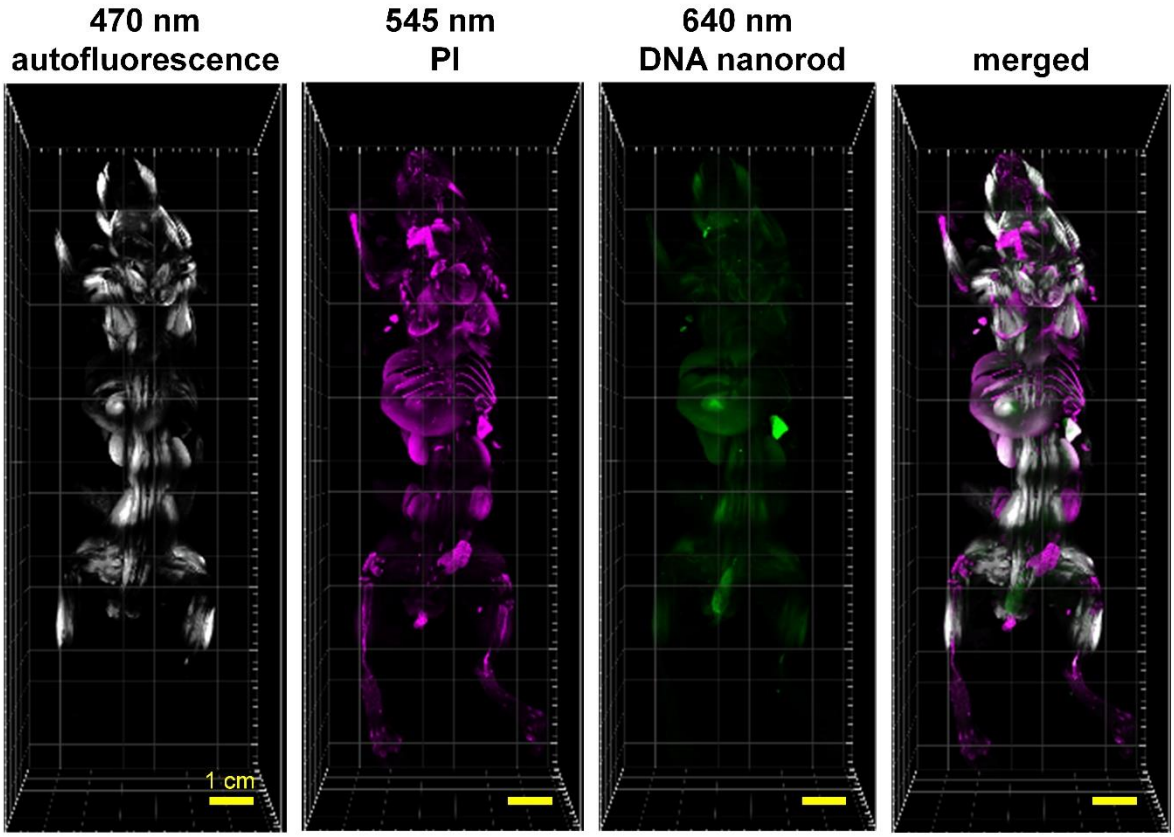

Figure 9 *In vivo* distribution of DNA-CX3CR1-Atto647N(4)-PP nanorod in CX3CR1-GFP mice
3D reconstruction of light sheet fluorescent microscope images of whole mouse after 20 min administration of DNA-CX3CR1-Atto647N(4)-PP nanorod (100 µL, 1 µM). White color showed autofluorescence signal indicating muscles. Magenta showed PI labeled cell neulei which were accumulated in inner organs and bone marrow. Green showed DNA nanorod signal that mainly accumulated in liver, spleen, lymph nod and stool.

Discussion

Over the last decades, the pharmaceutical industry faces unprecedented decline of proportion in approved drugs and experiences important challenges in business model, among which drug safety and efficacy are serious concerns since large amount of drug candidates fail in the preclinical or clinical stage[244]. To characterize the *in vivo* behaviors of drug candidates, virtual assessments by molecular imaging have played increasing role in diverse therapeutics development[245]. For systematic study, both of the drugs and imaging agents should be programmable to adjust the types, dose, addressability, release time and clearance to achieve the best therapy and the lowest side-effects. Recently, nanomaterial assisted drug delivery and monitoring are very promise to provide informative and accurate *in vivo* description and improve the evaluation of on-target and off-target effects of candidates. Especially, DNA origami nanotechnology has compelling advantages including excellent biocompatibility, structural programmability, functional designable and broad attachments tolerance.

Employing DNA nanotechnology as drug delivery nanovehicles have been studied for cancer treatment[246-248], gene silencing[249] and synergistic vaccines[250] in mice. These researches showed promising results, but applied simple design of nanostructure, provided little information about the administration dose and lacked cellular details of DNA cargo-cell interaction *in vivo*. It is well-known that there are several hurdles to bring DNA origami into *in vivo*. One of the greatest discourage factor is the high cost of mass production of origami up to gram with well-designed structures. The original single strand DNA material used in the formation are costly, as well as the equipment required to keep the design as delicate as possible. For example, the price of synthesized nanomachine of single gram is estimated around $100.1000[251]. in 2017, Dietz et.al. reported a scalable production and purification pipeline to generate several custom DNA origami using single-strand precursor DNA generated from bacteriophages in shaker-flask culture, which costed €180 per gram of nanorod[234]. This opened new possibility to systematically study the strategy of DNA origami as powerful platform for drug delivery and monitoring.

Before bring the mass-productive DNA nanrod for practical *in vivo* application, we assessed the immunogenicity, stability. Potential immune response of DNA origami architecture should be examined, because 90% of studies of DNA origami were fabricated from M13mp18 phage DNA[252]. In addition, the structural integrity of origami after exposing to the physiological medium and bodily fluids is important feature. Polymer coating has been shown to not only attenuate immune stimulation but also display enhanced permeability and retention effects[253]. By removing the residual exotoxin of *Escherichia coli* and poly(ethylene glycol)-poly(L-lysine) (PP) cationic polymer coating, the DNA nanrod are safe and stable enough for animal experiments by evaluating the acute and adaptive immune reactions and behavior performances.

Bare DAN origami would not bind to specific cell for targeting, antibody or aptamer was conjugated to DNA origami to bind to receptor-bearing cells and increase the efficacy[246]. As a prove-of-concept, we linked four Atto647N dyes and one CX3CR1 antibody at specific positons of DNA nanorod to comparatively investigate the targeting, clearance and biodistribution. Previously, visualizations of imaging agents are based on multimodality imaging, such as PET/CT, MRI-PET and so on. These readout methods are helpful to monitor the exogenous substrates in gross view, but also ambiguous in accuracy due to the low resolution. To closely observe and quantitatively study the DNA origami *in vivo* behaviors, we applied tissue clearing and imaging technology in whole body of mouse, which was more reliable and informative at cellular level. CX3CR1 antibody guided DNA origami mostly accumulated inside organs

hosting immune cells including spleen, liver, lymph node. DNA nanorod showed some extent stability in the circulation and well clearance after 24 hours.

In conclusion, here we proved a scalable production DNA nanorod could be safely used as drug delivery and monitoring system, whose *in vivo* behaviors were well and precisely characterized by tissue clearing and imaging technology at cellular resolution. This holds promising applications in evaluation and optimization of drug candidate to accelerate the whole development.

Materials and Methods

Animals:

Here described the animal lines and general cares for this study. Half-to-half mixed gender CD-1 IGS mice (stain code: 022) were brought from Charles River and CX3CR1-GFP-/+ (B6.129P-CX3CR1tm1Litt/J, strain code 005582) were bought from Jackson Laboratory. All of the mice were taken care by professional housing standard following 12-12 hours light-dark cycle. According to the institutional guidelines of Klinikum der Universität München / Ludwig Maximilian University of Munich, approved by the Ethical Review Board of the Government of Upper Bavaria (Regierung von Oberbayern, Munich, Germany) and the Animal Experiments Council under the Danish Ministry of Environment and Food (2015-15-0201-00535) and in accordance with the European directive 2010/63/EU for animal research, all animal experiments were performed legally and ethically. For each experiments, mice were grouped randomly. The transgenic mice used in the study were confirmed by genotyping and only the ones with positive expression of fluorescent protein were chosen for the experiments. All data are reported following the ARRIVE criteria.

Before scarified, the mice were gently treated with a mixture solution (MMF) composed by midazolam, medetomidine and fentanyl by intraperitoneal injection for deep anesthetization. The amount of dose for each component is 0.5 mg/kg, 5 mg/kg and 0.05 mg/kg of body weight. Once the mouse showed no pedal reflex by pinching the toe with tweezer, the legs of mouse were fixed using needles and the chest was exposed by careful cutting. A syringe was injected into the left ventricle of heart and the blood was extracted slowly. The spleen was collected. Around 4-5 payer's patches were dissected from the intestine. All samples were kept on ice. The animals were sacrificed afterwards. Animals for tissue clearing, a needle connecting with tubing were inserted into the intracardial site and the heparinized 0.01 M PBS solution (10 U ml−1 of heparin, Ratiopharm) was pumped into the whole body of moues using a Leica Perfusion One system setting with 110 mmHg pressure. The perfusion of PBS lasted for 5~10 minutes to wash out all the blood at room temperature, indicated by the liver color getting to

pale from dark red, then the perfusion solution was changed to 4% PFA for 10~20 min to fix the mouse body. The skin of mouse was peeled off and interested organs or whole body were dissected for post-fixation in 4% PFA at 4°C overnight. Then the collected organs or bodies were washed with 0.01 M PBS at room temperature, 3 times of 10 min incubation.

Injection of DNA Nanorod in Mice

All DNA nanorod origami were provided by Bionanotech & Molecular Robotics Lab at Technical University of Munich.

Mixed gender CD-1 mice were grouped randomly (n=5), then received tail-vein injection of $MgCl_2$ folding buffer, original DNA nanorod without further purification, DNA nanorod with purification to remove endotoxin and purified DNA nanorod coating with poly(ethylene glycol)-poly(L-lysine) (2 µM x 100 µL for each mouse). After 4 hours and 24 hours, the blood (0.5-1 mL) and spleen were collected and kept on ice.

Mixed gender CD-1 mice were grouped randomly (n=6), then received gavage injections of $MgCl_2$ folding buffer, poly(ethylene glycol)-poly(L-lysine) solution and purified DNA nanorod coating with poly(ethylene glycol)-poly(L-lysine) (2 µM x 400 µL for each mouse). After 4 hours and 7days animals were sacrificed, the blood (0.5-1 mL), spleen and payer's patches were collected and kept on ice. For 7 days groups mice, the body weight, body temperature and basic neurological tests were recorded at day 0, day 1, day 3, day 5 and day 7.

Catheters were made from polyethylene tubing (parameters of inner diameter of 0.28 mm and outer diameter of 0.61 mm) and were heated and pulled to obtain a cone-shaped tip with. Catheter tips were inspected under a stereo microscope (magnification, 31.5x; SZX 10, Olympus Schweiz, Volketswil, Switzerland). The tips of the catheters used had an outer diameter of 110 µm ± 30 µm (n = 12) and were angled by using a scalpel. Capillaries were flushed with sterile 0.9% NaCl. CX3CR1-GFP mice were grouped randomly (n=3) and were anesthetized by using 5% isoflurane (Forene, Abbott, Baar, Switzerland) in oxygen (300 mL/min). Anesthetized mice were laid on their backs on a heating pad (Horn, Gottmadingen, Germany), and the temperature of mice body was kept at 37 °C. During surgery, anesthesia was maintained by using an inspiratory isoflurane concentration of 2% to 3%. Surgery was performed under a stereo microscope (magnification, 31.5x; SZX 10, Olympus). The left femoral artery, vein, and nerve were exposed through a skin incision of 3 to 4 mm parallel and inferior to the inguinal ligament. The femoral vein was separated from surrounding tissue and the capillary was injected with the polyethylene tubing by advancing the thinned tip into the artery. A total volume of 100µl of 1µM $MgCl_2$ folding buffer ($MgCl_2$ buffer), 4µM Atto647N dye

and PP solution (Atto647N+PP), 1µM DNA-Atto647N(4)-PP and 1µM DNA-CX3CR1-Atto647N(4)-PP was delivered through this capillary for each mouse. Animals were sacrificed after 20 minutes, 4 hours or 24 after injection.

Sample Processing and Flow Cytometry Analysis.

Isolation of leukocytes from blood (without mesh steps), spleen and payer's patches: after harvest from mice, place them in PBS containing tubes on ice. Take a 50 mL tube and put a cell strainer of 40 µm pores on it. Place the sample on cell strainer and mesh them with 1 mL syringe plunger while continuously adding PBS on it (~20 ml). The cell strainer was rinsed with additional 5 mL PBS. The tubes were centrifuged at 500 g for 7 minutes at 15 °C. Examine the cell pellets in the bottom of tubes and discard the supernatants by tilting the tubes in sink. Add 2-3 mL of pre-warmed RBCs lysis buffer in the tubes and mix the cells. After 2 min of incubation at room temperature, to all tubes were added 20 mL of PBS and centrifuged at 500 g for 7 minutes at 15 °C. Wash the cells once with 1x PBS. Resolve cells in 1 mL of 1x PBS or FACS staining buffer and place the cells back on the ice. Count the cells using automated cell counter (1/100 dilution). Place approx. 106 per sample in a FACS tube (total volume 100 µl). Add antibody master mix (1/20 – 1/25 pre-dilution dependent on mAb). After an incubation of 30 min at 4°C in the dark. The samples were washed with 2 ml of PBS twice (500 g at 15 °C). Finally resolve cells in 100 µl (ready for acquisition).

The cell staining was done using commercialized anti-mouse antibodies as listed: anti-CD11c (clone: HL3, eBioscience), anti-MHC class II (clone: NIMR-4, eBioscience), anti-CD11b (clone: M1/70, eBioscience), anti-CD45 (clone: 30-F11, eBioscience), anti-CD4 (clone: RM4-5, eBioscience), anti-Ly6G (clone: RB6-8C5, eBioscience), anti-CD3 (clone: 17A2, eBioscience), anti-Ly6C (clone: HK1.4, eBioscience). The staining protocol were following the instruction of manufacturer. The staining samples were tested using a FACSverse flow cytometer (BD Biosciences) to collect the flow cytometric data. Later the analysis was conducted by FlowJo software (Treestar).

vDISCO Tissue Clearing

The experiments were modified from previous reports of the lab[240]. The labeling and clearing of CX3CR1-GFP mice followed vDISCO protocol. Here summarized as: "Generally, the process of whole mouse body was performed inside a glass chamber (Omnilab, 5163279) with a volume capacity of 300 ml to immersing the full body completely. A transcardialcirculatory system was set up using a peristaltic pump (ISMATEC, REGLO Digital MS-4/8 ISM 834) and connected tubing (SC0266) with one open end to suck the solution in the glass chamber and one sealed end of needle to insert into the heart of mouse. The pump pressure was kept at

160 mmHg (45 r.p.m.). The sealed end of tubing was linked with a short cutting of 1 ml syringe duct (Braun, 9166017V) and the syringe was held with a needle (Leica, 39471024) that could pass the nanobody-sized particles. This needle was injected into the heart and further sealed and protected by a drop of superglue (Pattex, PSK1C) sticking at the needle insertion site. Using this system, 250 ml of PBS washing, decolorization solution, decalcification solution and again PBS washing solutions were refreshed several times at room temperature until the mouse was soft, white color. Then perfusion solution was changed to 250 ml of permeabilization solution to loosen the tissue extracellular matrix, followed by a refreshed permeabilization solution added with 290 µl of PI (1 mg/ml stock) to label the cell nuclei. After that, the mice were washed with washing solution. Next, the animals were ready for 3DISCO-modified whole-body clearing protocol by passive incubation. The chamber with mice were gently shaking on a rocker (IKA, 2D digital) kept inside of a fume hood. For clearing, the dehydration was done to get rid of the tissue water by incubation with gradient increased THF/water mixtures: 50%, 70%, 80%, 100% x 2 times. The THF/water mixture solution was about 200 ml each step and lasted for 12h at room temperature. Then the delipidation solution of dichloromethane was continued for 3h to remove the tissue lipid. In the end, the RI matching solution of BABB was applied to make the whole mouse body transparent after overnight incubation. During the whole clearing process, to avoid the evaporation of organic solutions, parafilm was used to seal the glass chamber, together with a covering of aluminum foil to prevent light exposure of fluorescent signal."

Light-sheet Microscopy Imaging

The process was briefly intruded according to our previous work[240]. Here summarized as: "Two light sheet microscopes were used from LaVision BioTec: commercialized Ultramicroscope II and a prototype Ultramicroscope. The Ultramicroscope II was designed with four filter channels: ex 470/40 nm-em 535/50 nm; ex 545/25 nm-em 605/70 nm; ex 580/25 nm-em 625/30 nm; ex 640/40 nm-em 690/50 nm. The prototype Ultramicroscope was attached with four filter channels: ex 470 nm-em 525/50 nm; ex 561 nm-em 595/40 nm; ex 640 nm-em 680/30 nm; ex 785 nm-em 845/55 nm. All microscopes could be set with multiple types of objectives. For mouse whole body imaging, Olympus air objective (Olympus MV PLAPO 1x/0.25 NA [WD = 65mm]) was used after coupling with an Olympus MVX10 zoom body. Optionally, objective (LaVision BioTec MI PLAN 1.1x/0.1 NA [WD = 17 mm]) was used after coupling with an Olympus revolving zoom body unit (U-TVCAC). If needed, interested organs dissected from the imaged whole mouse could be reimaged with high magnification objectives, for example: Olympus XLFLUOR 4x objective (corrected/0.28 NA [WD = 10 mm]) and LaVision BioTec MI PLAN 12x objective (0.53 NA [WD = 10 mm]). All of the Image stacks were taken by adjusting the following parameters: the overlapping percentage of mosaic scans was set to 20%-30%

for both of the longitudinal x-axis and y-axis directions; the jumping of z-step was set to 3-8 μm; the laser power was adjusted depending on the overview intensity of the fluorescent signal to avoid saturation; the exposure time with defined laser power was set at 90-120 ms to achieve fast imaging; the light-sheet width was set at 70-80% to covering large FOV with fine resolution."

Immunostaining and Laser-scanning Confocal Microscopy Imaging

Additionally, to identify the cells swollen DNA nanorod, liver organs were rehydrated following DCM, 100% THF, 70% THF, 50% THF and PBS x 2 times steps. The rehydrated livers were sliced with vibratome (Leica, VT1200S) to collect several 1mm thick sections for immunostaining. These sections were blocked with blocking buffer at room temperature for 2-3 hours, a mixture of 10% goat serum, 10% DMSO (Roth, A994.2) and 0.2% Triton X-100 in PBS. 1 ml of primary antibody solution was added in a 24-well plate to the sections for 2 hours at 37 °C: rabbit antibody anti-Iba1 (1:1000, 019-19741, Wako) dissolved in the buffer of 10mg·L-1Heparin, 3% goat serum, 0.2%Tween-20, 3% DMSO in PBS. After three times of washing with a washing buffer containing only 0.2%Tween-20 and 10mg·L-1Heparin in PBS. Alexa 470-conjugated secondary antibodies (1:500, Thermo Fisher) was applied to the sample dissolved in the same buffer of primary antibody. After washing with PBS, the samples were ready for imaging. The imaging was following previous work, as summarized: "All confocal images were conducted with Zeiss LSM 880 confocal microscope mounted with a 40x oil-immersion objective (Zeiss, ECPlan-NeoFluar × 40/1.30 oil DIC M27, 1.3 NA [WD = 0.21 mm]) for higher magnification. Cleared samples were placed on the glass bottom of MatTek petri dishes (35 mm) and immersed in several drops of BABB solution to keep the tissue transparency. All Images was analyzed using Zen 2 software (v.10.0.4.910; Carl Zeiss AG)."

Image Processing

The imaging processing was modified from previous work[240]. It was described as: "Laboratory HP workstation Z840 (RAM of 196 GB, 8 core Xeon processor, Nvidia Quadro k5000 graphics card) and HP workstation Z840 (DDR4 RAM of 256 GB, dual Xeon processor, nVidia Quadro M5000 8GB graphic card) were used for data processing, analysis and 3D visualization. Specifically, Fiji, Imaris (v.9.1, Bitplane) and Arivis were installed to show the 3D and 2D data. In general, software ImSpector (v.5.295, LaVision BioTec) of light-sheet microscope would give all raw TIFF images of 16-bit grayscale size from each channel separately. The raw TIFF images from mosaic scans were loaded in Fiji and stitched by plugin 49 to generate tiled images from each channel and outputted in same TIFF format. All TIFF images could be compressed in LZW format to save space and increase data processing speed. The stitched TIFF files of each channel and each part of whole body scans were loaded in Arivis software

(Vision4D, v.2.12.6 × 64) and started to fuse into one whole block. Typically, 3 similar landmarks were manually chosen from each of neighboring stacks according to anatomic characters to align the overlapping region and then infuse the two stacks into one stack. The same process was repeated to sequentially finish the whole body fusion. It is easier to identify the same landmarks if choosing unique cellular structures or specific vessel structures. It is common that obvious border lines (e.g. dimmer) will show up in some stitching images of mesoscale light-sheet imaging, which is caused by the repeated scanning of overlapping region of two tiles. That could reduce the signal intensity of borders. In addition, there are missing images of certain channel at certain tile, or one of the blocks are brighter or darker than the others. This happens during the long-term (e.g. 2-3 days) of non-stopping scans. However, such artefacts would not heavily impede the 3D visualization at gross view. Finishing the 3D fusion, the Arivis would output the TIFF images of whole mouse, which could be loaded in Imaris for further visualization, video-making, maximum-intensity projection."

Statistical Analysis

Data were loaded and analyzed by GraphPad Prism software with version 6.0. One-way analysis of variance (ANOVA) was used to analyze each group of normally distributed data and multiple comparisons was set for P values readout.

REFERENCES

1 Ponten, F., Jirstrom, K. & Uhlen, M. The Human Protein Atlas--a tool for pathology. *The Journal of pathology* **216**, 387-393, doi:10.1002/path.2440 (2008).

2 Sherif, T. *et al.* CBRAIN: a web-based, distributed computing platform for collaborative neuroimaging research. *Frontiers in neuroinformatics* **8**, 54, doi:10.3389/fninf.2014.00054 (2014).

3 Regev, A. *et al.* The Human Cell Atlas. *eLife* **6**, doi:10.7554/eLife.27041 (2017).

4 Hu, B. C. The human body at cellular resolution: the NIH Human Biomolecular Atlas Program. *Nature* **574**, 187-192, doi:10.1038/s41586-019-1629-x (2019).

5 Lauterbur, P. C. Image formation by induced local interactions. Examples employing nuclear magnetic resonance. 1973. *Clinical orthopaedics and related research*, 3-6 (1989).

6 Mansfield, P. & Grannell, P. K. NMR'diffraction'in solids? *Journal of Physics C: solid state physics* **6**, L422 (1973).

7 Steward, T. *et al.* A multimodal MRI study of the neural mechanisms of emotion regulation impairment in women with obesity. *Translational psychiatry* **9**, 1-10 (2019).

8 Giedd, J. N. *et al.* Brain development during childhood and adolescence: a longitudinal MRI study. *Nature neuroscience* **2**, 861 (1999).

9 Ladd, M. E. *et al.* Pros and cons of ultra-high-field MRI/MRS for human application. *Progress in nuclear magnetic resonance spectroscopy* **109**, 1-50, doi:10.1016/j.pnmrs.2018.06.001 (2018).

10 Wang, S. *et al.* Quantitative assessment of myelination patterns in preterm neonates using T2-weighted MRI. *Scientific reports* **9**, 1-12 (2019).

11 Sijens, P. E., Edens, M. A., Bakker, S. J. & Stolk, R. P. MRI-determined fat content of human liver, pancreas and kidney. *World journal of gastroenterology: WJG* **16**, 1993 (2010).

12 Craddock, R. C. *et al.* Imaging human connectomes at the macroscale. *Nat Methods* **10**, 524-539 (2013).

13 Edlow, B. L. *et al.* 7 Tesla MRI of the ex vivo human brain at 100 micron resolution. *Scientific data* **6**, 244, doi:10.1038/s41597-019-0254-8 (2019).

14 Nowogrodzki, A. The strongest scanners. *Nature* **563**, 24-26 (2018).

15 Raab, S. S. The current and ideal state of anatomic pathology patient safety. *Diagnosis* **1**, 95-97, doi:10.1515/dx-2013-0031 (2014).

16 Rosai, J. Why microscopy will remain a cornerstone of surgical pathology. *Laboratory investigation; a journal of technical methods and pathology* **87**, 403-408, doi:10.1038/labinvest.3700551 (2007).

17 Masters, B. R. in *ENCYCLOPEDIA OF LIFE SCIENCES* (2008).

18 Titford, M. A Short History of Histopathology Technique. *Journal of Histotechnology* **29**, 99-110, doi:10.1179/his.2006.29.2.99 (2006).

19 John, H. The Construction of Timber, from its early growth; Explained by Microscope, and proven from Experiments, in a great Variety of Kinds. 5–11 (1770).

20 KUHLMANN, W. D. Microtomy of tissue specimens, collection of sections. (2018).

21 Lang, G. Histotechnik. Praxislehrbuch für die Biomedizinische Analytik. (2006).

22 Alturkistani, H. A., Tashkandi, F. M. & Mohammedsaleh, Z. M. Histological Stains: A Literature Review and Case Study. *Global journal of health science* **8**, 72-79, doi:10.5539/gjhs.v8n3p72 (2015).
23 Costa, C. A., De Brito, K. N., Gomes, M. A. & Caliari, M. V. Histopathological and immunohistochemical study of the hepatic lesions experimentally induced by Entamoeba dispar. *European journal of histochemistry : EJH* **54**, e39 (2010).
24 Titford, M. Progress in the Development of Microscopical Techniques for Diagnostic Pathology. *Journal of Histotechnology* **32**, 9-19, doi:10.1179/his.2009.32.1.9 (2009).
25 Beer, J. J. The Emergence of the German Dye Industry. *University of Illinois Press* (1959).
26 Musumeci, G. Past, present and future: overview on histology and histopathology. *Journal of Histology and Histopathology* **1**, doi:10.7243/2055-091x-1-5 (2014).
27 Titford, M. The long history of hematoxylin. *Biotechnic & Histochemistry* **80**, 73-78, doi:10.1080/10520290500138372 (2005).
28 Drury, R. A. B. Theory and Practice of Histotechnology. *J Clin Pathol* **34**, 1406-1406 (1981).
29 Marrack, J. Nature of Antibodies. *Nature* **133**, 292-293, doi:10.1038/133292b0 (1934).
30 The Chemistry of Antigens and Antibodies. *Nature* **142**, 316-316, doi:10.1038/142316c0 (1938).
31 Coons, A. H., Creech, H. J. & Jones, R. N. Immunological Properties of an Antibody Containing a Fluorescent Group. *Proceedings of the Society for Experimental Biology and Medicine* **47**, 200-202, doi:10.3181/00379727-47-13084p (1941).
32 Childs, G. V. in *Pathobiology of Human Disease* (eds Linda M. McManus & Richard N. Mitchell) 3775-3796 (Academic Press, 2014).
33 Gorris, M. A. J. *et al.* Eight-Color Multiplex Immunohistochemistry for Simultaneous Detection of Multiple Immune Checkpoint Molecules within the Tumor Microenvironment. *The Journal of Immunology* **200**, 347, doi:10.4049/jimmunol.1701262 (2018).
34 Clarke, T. Mice make medical history. *Nature*, doi:10.1038/news021202-10 (2002).
35 Castle, W. E. & Little, C. C. On a Modified Mendelian Ratio among Yellow Mice. *Science* **32**, 868-870, doi:10.1126/science.32.833.868 (1910).
36 Chalfie, M., Tu, Y., Euskirchen, G., Ward, W. W. & Prasher, D. C. Green fluorescent protein as a marker for gene expression. *Science* **263**, 802-805, doi:10.1126/science.8303295 (1994).
37 Okabe, M., Ikawa, M., Kominami, K., Nakanishi, T. & Nishimune, Y. 'Green mice' as a source of ubiquitous green cells. *FEBS Letters* **407**, 313-319, doi:10.1016/s0014-5793(97)00313-x (1997).
38 Abe, T. & Fujimori, T. Reporter Mouse Lines for Fluorescence Imaging. *Development, Growth & Differentiation* **55**, 390-405, doi:10.1111/dgd.12062 (2013).
39 Weissman, T. A. & Pan, Y. A. Brainbow: new resources and emerging biological applications for multicolor genetic labeling and analysis. *Genetics* **199**, 293-306, doi:10.1534/genetics.114.172510 (2015).

40 Kawano, F., Okazaki, R., Yazawa, M. & Sato, M. A photoactivatable Cre-loxP recombination system for optogenetic genome engineering. *Nature chemical biology* **12**, 1059-1064, doi:10.1038/nchembio.2205 (2016).
41 Antonie van Leeuwenhoek, S. H. The select works of Antony van Leeuwenhoek : containing his microscopical discoveries in many of the works of nature. (1800).
42 Hooke, R. Micrographia: or some physiological descriptions of minute bodies made by magnifying glasses, with observations and inquiries thereupon. (1665).
43 Masters, B. R. History of the Optical Microscope in Cell Biology and Medicine. *eLS*, doi:doi:10.1002/9780470015902.a0003082

10.1002/9780470015902.a0003082 (2008).
44 Zernike, F. How I Discovered Phase Contrast. *Science* **121**, 345-349, doi:10.1126/science.121.3141.345 (1955).
45 Zernike, F. Phase contrast, a new method for the microscopic observation of transparent objects. *Physica* **9**, 686-698, doi:https://doi.org/10.1016/S0031-8914(42)80035-X (1942).
46 Smith, F. H. Microscopic interferometry. *Research (London)* **8**, 385–395 (1955).
47 Nomarski, G. & Weill, A. R. Application à la métallographie des méthodes interférentielles à deux ondes polarisées. *Rev. Met. Paris* **52**, 121-134 (1955).
48 Rusk, N. The fluorescence microscope. *Nature Cell Biology* **11**, S8-S9, doi:10.1038/ncb1941 (2009).
49 Ploem, J. S. The use of a vertical illuminator with interchangeable dichroic mirrors for fluorescence microscopy with incidental light. *Zeitschrift fur wissenschaftliche Mikroskopie und mikroskopische Technik* **68**, 129-142 (1967).
50 Wollman, A. J., Nudd, R., Hedlund, E. G. & Leake, M. C. From Animaculum to single molecules: 300 years of the light microscope. *Open biology* **5**, 150019, doi:10.1098/rsob.150019 (2015).
51 Siedentopf, H. & Zsigmondy, R. Uber sichtbarmachung und größenbestimmung ultramikoskopischer teilchen, mit besonderer anwendung auf goldrubingläser. *Annalen der Physik* **315**, 1-39 (1902).
52 Huisken, J., Swoger, J., Del Bene, F., Wittbrodt, J. & Stelzer, E. H. Optical sectioning deep inside live embryos by selective plane illumination microscopy. *Science* **305**, 1007-1009, doi:10.1126/science.1100035 (2004).
53 Santi, P. A. Light sheet fluorescence microscopy: a review. *The journal of histochemistry and cytochemistry : official journal of the Histochemistry Society* **59**, 129-138, doi:10.1369/0022155410394857 (2011).
54 Schneider, M. V. & Orchard, S. in *Bioinformatics for omics Data* 3-30 (Springer, 2011).
55 Vailati-Riboni, M., Palombo, V. & Loor, J. J. in *Periparturient Diseases of Dairy Cows* 1-7 (Springer, 2017).
56 Perez-Riverol, Y. *et al.* Quantifying the impact of public omics data. *Nature communications* **10**, 1-10 (2019).
57 Manzoni, C. *et al.* Genome, transcriptome and proteome: the rise of omics data and their integration in biomedical sciences. *Briefings in bioinformatics* **19**, 286-302 (2016).
58 Karczewski, K. J. & Snyder, M. P. Integrative omics for health and disease. *Nature Reviews Genetics* **19**, 299 (2018).

59 Hasin, Y., Seldin, M. & Lusis, A. Multi-omics approaches to disease. *Genome biology* **18**, 83 (2017).
60 Hu, Y. *et al.* Single cell multi-omics technology: methodology and application. *Frontiers in cell and developmental biology* **6**, 28 (2018).
61 Kiselev, V. Y., Andrews, T. S. & Hemberg, M. Challenges in unsupervised clustering of single-cell RNA-seq data. *Nature Reviews Genetics*, 1 (2019).
62 Gawad, C., Koh, W. & Quake, S. R. Single-cell genome sequencing: current state of the science. *Nature Reviews Genetics* **17**, 175 (2016).
63 Martorell-Marugán, J. *et al.* in *Computational Biology [Internet]* (Codon Publications, 2019).
64 Zhang, Z. *et al.* Deep learning in omics: a survey and guideline. *Briefings in functional genomics* **18**, 41-57 (2018).
65 Najafabadi, M. M. *et al.* Deep learning applications and challenges in big data analytics. *Journal of Big Data* **2**, 1 (2015).
66 LeCun, Y., Bengio, Y. & Hinton, G. Deep learning. *Nature* **521**, 436-444, doi:10.1038/nature14539 (2015).
67 Zhavoronkov, A. *et al.* Deep learning enables rapid identification of potent DDR1 kinase inhibitors. *Nature biotechnology* **37**, 1038-1040 (2019).
68 Wallach, I., Dzamba, M. & Heifets, A. AtomNet: a deep convolutional neural network for bioactivity prediction in structure-based drug discovery. *arXiv preprint arXiv:1510.02855* (2015).
69 Krizhevsky, A., Sutskever, I. & Hinton, G. E. in *Advances in neural information processing systems.* 1097-1105.
70 Todorov, M. I. *et al.* Automated analysis of whole brain vasculature using machine learning. *bioRxiv*, 613257 (2019).
71 Pan, C. *et al.* Deep Learning Reveals Cancer Metastasis and Therapeutic Antibody Targeting in the Entire Body. *Cell* **179**, 1661-1676. e1619 (2019).
72 Godec, P. *et al.* Democratized image analytics by visual programming through integration of deep models and small-scale machine learning. *Nature communications* **10**, 1-7 (2019).
73 Amodio, M. *et al.* Exploring single-cell data with deep multitasking neural networks. *BioRxiv*, 237065 (2019).
74 Choi, E., Schuetz, A., Stewart, W. F. & Sun, J. Using recurrent neural network models for early detection of heart failure onset. *Journal of the American Medical Informatics Association* **24**, 361-370 (2016).
75 Tian, T., Wan, J., Song, Q. & Wei, Z. Clustering single-cell RNA-seq data with a model-based deep learning approach. *Nature Machine Intelligence* **1**, 191 (2019).
76 Woodard, H. Q. & White, D. R. The composition of body tissues. *The British journal of radiology* **59**, 1209-1218, doi:10.1259/0007-1285-59-708-1209 (1986).
77 Genina, E. A., Bashkatov, A. N. & Tuchin, V. V. Tissue optical immersion clearing. *Expert review of medical devices* **7**, 825-842, doi:10.1586/erd.10.50 (2010).
78 Tainaka, K., Kuno, A., Kubota, S. I., Murakami, T. & Ueda, H. R. Chemical Principles in Tissue Clearing and Staining Protocols for Whole-Body Cell Profiling. *Annual review of cell and developmental biology* **32**, 713-741, doi:10.1146/annurev-cellbio-111315-125001 (2016).
79 Jacques, S. L. Optical properties of biological tissues: a review. *Physics in medicine and biology* **58**, R37-61, doi:10.1088/0031-9155/58/11/R37 (2013).

80 Richardson, D. S. & Lichtman, J. W. Clarifying Tissue Clearing. *Cell* **162**, 246-257, doi:10.1016/j.cell.2015.06.067 (2015).
81 Krishna, R., Unsworth, T. J. & Edge, R. in *Reference Module in Materials Science and Materials Engineering* (Elsevier, 2016).
82 Dunn, A. K. in *Optical Imaging of Neocortical Dynamics* 33-51 (Springer, 2014).
83 Tsai, P. S. *et al.* Plasma-mediated ablation: an optical tool for submicrometer surgery on neuronal and vascular systems. *Current opinion in biotechnology* **20**, 90-99, doi:10.1016/j.copbio.2009.02.003 (2009).
84 Seiriki, K. *et al.* High-Speed and Scalable Whole-Brain Imaging in Rodents and Primates. *Neuron* **94**, 1085-1100 e1086, doi:10.1016/j.neuron.2017.05.017 (2017).
85 Helmchen, F. & Denk, W. Deep tissue two-photon microscopy. *Nat Methods* **2**, 932-940, doi:10.1038/nmeth818 (2005).
86 Kim, S. Y., Chung, K. & Deisseroth, K. Light microscopy mapping of connections in the intact brain. *Trends in cognitive sciences* **17**, 596-599, doi:10.1016/j.tics.2013.10.005 (2013).
87 Becker, K., Jahrling, N., Saghafi, S. & Dodt, H. U. Ultramicroscopy: light-sheet-based microscopy for imaging centimeter-sized objects with micrometer resolution. *Cold Spring Harbor protocols* **2013**, 704-713, doi:10.1101/pdb.top076539 (2013).
88 Luft, J. H. Improvements in epoxy resin embedding methods. *The Journal of biophysical and biochemical cytology* **9**, 409-414, doi:10.1083/jcb.9.2.409 (1961).
89 An, Y. H., Moreira, P. L., Kang, Q. K. & Gruber, H. E. in *Handbook of Histology Methods for Bone and Cartilage* 185-197 (Springer, 2003).
90 Alwahaibi, N., Aljaradi, S. & Alazri, H. Alternative to xylene as a clearing agent in histopathology. *Journal of laboratory physicians* **10**, 189 (2018).
91 Werner, S. Über das Durchsichtigmachen von menschlichen und tierischen Präparaten und seine theoretischen Bedingungen, nebst Anhang. (1914).
92 Orsini, M. W. Technique of preparation, study and photography of benzyl-benzoate cleared material for embryological studies. *Journal of reproduction and fertility* **3**, 283-287 (1962).
93 Ljetnik, S. Eine variation der spalteholzschen methode. *Anat. Anz*, 201–202 (1924).
94 F Eitel, R. S., B Hohn, L Schweiberer. Präparationstechnische Weiterentwicklung und Standardisierung der mikroangiographischen Untersuchungsmethode nach Spalteholz. *Der Unfallchirurg* **89**, 326–336 (1986).
95 Steinke, H. & Wolff, W. A modified Spalteholz technique with preservation of the histology. *Annals of anatomy = Anatomischer Anzeiger : official organ of the Anatomische Gesellschaft* **183**, 91-95, doi:10.1016/S0940-9602(01)80020-0 (2001).
96 von Hagens, G., Tiedemann, K. & Kriz, W. The current potential of plastination. *Anatomy and embryology* **175**, 411-421 (1987).
97 Howat, W. J. & Wilson, B. A. Tissue fixation and the effect of molecular fixatives on downstream staining procedures. *Methods* **70**, 12-19, doi:10.1016/j.ymeth.2014.01.022 (2014).
98 Cham, B. E. & Knowles, B. A solvent system for delipidation of plasma or serum without protein precipitation. *Journal of lipid research* **17**, 176-181 (1976).

99 Dodt, H. U. *et al.* Ultramicroscopy: three-dimensional visualization of neuronal networks in the whole mouse brain. *Nat Methods* **4**, 331-336, doi:10.1038/nmeth1036 (2007).
100 Doyle, A., McGarry, M. P., Lee, N. A. & Lee, J. J. The construction of transgenic and gene knockout/knockin mouse models of human disease. *Transgenic research* **21**, 327-349, doi:10.1007/s11248-011-9537-3 (2012).
101 Day, R. N. & Davidson, M. W. The fluorescent protein palette: tools for cellular imaging. *Chemical Society reviews* **38**, 2887-2921, doi:10.1039/b901966a (2009).
102 Qi, Y. *et al.* FDISCO: Advanced solvent-based clearing method for imaging whole organs. *Science advances* **5**, eaau8355, doi:10.1126/sciadv.aau8355 (2019).
103 Schwarz, M. K. *et al.* Fluorescent-protein stabilization and high-resolution imaging of cleared, intact mouse brains. *PloS one* **10**, e0124650, doi:10.1371/journal.pone.0124650 (2015).
104 Klingberg, A. *et al.* Fully Automated Evaluation of Total Glomerular Number and Capillary Tuft Size in Nephritic Kidneys Using Lightsheet Microscopy. *Journal of the American Society of Nephrology : JASN* **28**, 452-459, doi:10.1681/ASN.2016020232 (2017).
105 Henning, Y., Osadnik, C. & Malkemper, E. P. EyeCi: Optical clearing and imaging of immunolabeled mouse eyes using light-sheet fluorescence microscopy. *Experimental eye research* **180**, 137-145, doi:10.1016/j.exer.2018.12.001 (2019).
106 Li, Y., Xu, J., Wan, P., Yu, T. & Zhu, D. Optimization of GFP fluorescence preservation by modified uDISCO clearing protocol. *Front Neuroanat* **12**, 67 (2018).
107 Becker, K., Jahrling, N., Saghafi, S., Weiler, R. & Dodt, H. U. Chemical clearing and dehydration of GFP expressing mouse brains. *PloS one* **7**, e33916, doi:10.1371/journal.pone.0033916 (2012).
108 Erturk, A. *et al.* Three-dimensional imaging of the unsectioned adult spinal cord to assess axon regeneration and glial responses after injury. *Nature medicine* **18**, 166-171, doi:10.1038/nm.2600 (2011).
109 Erturk, A. *et al.* Three-dimensional imaging of solvent-cleared organs using 3DISCO. *Nature protocols* **7**, 1983-1995, doi:10.1038/nprot.2012.119 (2012).
110 Žygelytė, E. *et al.* RetroDISCO: clearing technique to improve quantification of retrograde labeled motor neurons of intact mouse spinal cords. *Journal of neuroscience methods* **271**, 34-42 (2016).
111 Pan, C. *et al.* Shrinkage-mediated imaging of entire organs and organisms using uDISCO. *Nat Methods* **13**, 859-867, doi:10.1038/nmeth.3964 (2016).
112 Hahn, C. *et al.* High-resolution imaging of fluorescent whole mouse brains using stabilised organic media (sDISCO). *Journal of biophotonics* **12**, e201800368, doi:10.1002/jbio.201800368 (2019).
113 Renier, N. *et al.* iDISCO: a simple, rapid method to immunolabel large tissue samples for volume imaging. *Cell* **159**, 896-910, doi:10.1016/j.cell.2014.10.010 (2014).
114 Renier, N. *et al.* Mapping of Brain Activity by Automated Volume Analysis of Immediate Early Genes. *Cell* **165**, 1789-1802, doi:10.1016/j.cell.2016.05.007 (2016).
115 Jing, D. *et al.* Tissue clearing of both hard and soft tissue organs with the PEGASOS method. *Cell research* **28**, 803-818, doi:10.1038/s41422-018-0049-z (2018).

116 Hama, H. *et al.* Scale: a chemical approach for fluorescence imaging and reconstruction of transparent mouse brain. *Nat Neurosci* **14**, 1481-1488, doi:10.1038/nn.2928 (2011).
117 Yu, T. *et al.* RTF: a rapid and versatile tissue optical clearing method. *Scientific reports* **8**, 1964 (2018).
118 Kuwajima, T. *et al.* ClearT: a detergent-and solvent-free clearing method for neuronal and non-neuronal tissue. *Development* **140**, 1364-1368 (2013).
119 Zhu, J. *et al.* MACS: Rapid aqueous clearing system for three-dimensional mapping of intact organs. *bioRxiv*, 832733 (2019).
120 Economo, M. N. *et al.* A platform for brain-wide imaging and reconstruction of individual neurons. *eLife* **5**, e10566 (2016).
121 Hama, H. *et al.* ScaleS: an optical clearing palette for biological imaging. *Nat Neurosci* **18**, 1518-1529, doi:10.1038/nn.4107 (2015).
122 Chen, L. *et al.* UbasM: An effective balanced optical clearing method for intact biomedical imaging. *Sci Rep* **7**, 12218, doi:10.1038/s41598-017-12484-3 (2017).
123 Susaki, E. A. & Ueda, H. R. Whole-body and Whole-Organ Clearing and Imaging Techniques with Single-Cell Resolution: Toward Organism-Level Systems Biology in Mammals. *Cell chemical biology* **23**, 137-157, doi:10.1016/j.chembiol.2015.11.009 (2016).
124 Staudt, T., Lang, M. C., Medda, R., Engelhardt, J. & Hell, S. W. 2,2'-thiodiethanol: a new water soluble mounting medium for high resolution optical microscopy. *Microscopy research and technique* **70**, 1-9, doi:10.1002/jemt.20396 (2007).
125 Aoyagi, Y., Kawakami, R., Osanai, H., Hibi, T. & Nemoto, T. A rapid optical clearing protocol using 2,2'-thiodiethanol for microscopic observation of fixed mouse brain. *PloS one* **10**, e0116280, doi:10.1371/journal.pone.0116280 (2015).
126 Costantini, I. *et al.* A versatile clearing agent for multi-modal brain imaging. *Sci Rep* **5**, 9808, doi:10.1038/srep09808 (2015).
127 Appleton, P. L., Quyn, A. J., Swift, S. & Nathke, I. Preparation of wholemount mouse intestine for high-resolution three-dimensional imaging using two-photon microscopy. *Journal of microscopy* **234**, 196-204, doi:10.1111/j.1365-2818.2009.03163.x (2009).
128 Musielak, T. J., Slane, D., Liebig, C. & Bayer, M. A Versatile Optical Clearing Protocol for Deep Tissue Imaging of Fluorescent Proteins in Arabidopsis thaliana. *PloS one* **11**, e0161107, doi:10.1371/journal.pone.0161107 (2016).
129 Costantini, I. *et al.* in *Optics in the Life Sciences.* BrM3B.2 (Optical Society of America).
130 Ke, M. T., Fujimoto, S. & Imai, T. SeeDB: a simple and morphology-preserving optical clearing agent for neuronal circuit reconstruction. *Nat Neurosci* **16**, 1154-1161, doi:10.1038/nn.3447 (2013).
131 Hou, B. *et al.* Scalable and DiI-compatible optical clearance of the mammalian brain. *Front Neuroanat* **9**, 19, doi:10.3389/fnana.2015.00019 (2015).
132 Susaki, E. A. *et al.* Whole-brain imaging with single-cell resolution using chemical cocktails and computational analysis. *Cell* **157**, 726-739 (2014).
133 Tainaka, K. *et al.* Chemical landscape for tissue clearing based on hydrophilic reagents. *Cell reports* **24**, 2196-2210. e2199 (2018).
134 Tainaka, K. *et al.* Whole-body imaging with single-cell resolution by tissue decolorization. *Cell* **159**, 911-924 (2014).

135 Kubota, S. I. *et al.* Whole-body profiling of cancer metastasis with single-cell resolution. *Cell reports* **20**, 236-250 (2017).
136 Murakami, T. C. *et al.* A three-dimensional single-cell-resolution whole-brain atlas using CUBIC-X expansion microscopy and tissue clearing. *Nature neuroscience* **21**, 625 (2018).
137 Pende, M. *et al.* High-resolution ultramicroscopy of the developing and adult nervous system in optically cleared Drosophila melanogaster. *Nature communications* **9**, 4731, doi:10.1038/s41467-018-07192-z (2018).
138 Zhu, X. *et al.* Ultrafast optical clearing method for three-dimensional imaging with cellular resolution. *Proceedings of the National Academy of Sciences of the United States of America* **116**, 11480-11489, doi:10.1073/pnas.1819583116 (2019).
139 Chung, K. *et al.* Structural and molecular interrogation of intact biological systems. *Nature* **497**, 332 (2013).
140 Chung, K. & Deisseroth, K. CLARITY for mapping the nervous system. *Nature methods* **10**, 508 (2013).
141 Magliaro, C. *et al.* Clarifying CLARITY: quantitative optimization of the diffusion based delipidation protocol for genetically labeled tissue. *Frontiers in neuroscience* **10**, 179 (2016).
142 Tomer, R., Ye, L., Hsueh, B. & Deisseroth, K. Advanced CLARITY for rapid and high-resolution imaging of intact tissues. *Nature protocols* **9**, 1682 (2014).
143 Swaney, J. *et al.* Scalable image processing techniques for quantitative analysis of volumetric biological images from light-sheet microscopy. *BioRxiv*, 576595 (2019).
144 Lee, E. *et al.* ACT-PRESTO: Rapid and consistent tissue clearing and labeling method for 3-dimensional (3D) imaging. *Sci Rep* **6**, 18631, doi:10.1038/srep18631 (2016).
145 Park, Y.-G. *et al.* Protection of tissue physicochemical properties using polyfunctional crosslinkers. *Nature biotechnology* **37**, 73 (2019).
146 Roy, D. S. *et al.* Brain-wide mapping of contextual fear memory engram ensembles supports the dispersed engram complex hypothesis. *bioRxiv*, 668483 (2019).
147 Yun, D. H. *et al.* Ultrafast immunostaining of organ-scale tissues for scalable proteomic phenotyping. *bioRxiv*, 660373 (2019).
148 Murray, E. *et al.* Simple, scalable proteomic imaging for high-dimensional profiling of intact systems. *Cell* **163**, 1500-1514 (2015).
149 Yang, B. *et al.* Single-cell phenotyping within transparent intact tissue through whole-body clearing. *Cell* **158**, 945-958 (2014).
150 Neckel, P. H., Mattheus, U., Hirt, B., Just, L. & Mack, A. F. Large-scale tissue clearing (PACT): Technical evaluation and new perspectives in immunofluorescence, histology, and ultrastructure. *Scientific reports* **6**, 34331 (2016).
151 Treweek, J. B. *et al.* Whole-body tissue stabilization and selective extractions via tissue-hydrogel hybrids for high-resolution intact circuit mapping and phenotyping. *Nature protocols* **10**, 1860 (2015).
152 Woo, J., Lee, M., Seo, J. M., Park, H. S. & Cho, Y. E. Optimization of the optical transparency of rodent tissues by modified PACT-based passive clearing. *Experimental & molecular medicine* **48**, e274 (2016).
153 Loren, M., Crouzet, C., Bahani, A., Vasilevko, V. & Choi, B. Optical clearing potential of immersion-based agents applied to thick mouse brain sections. *PloS one* **14**, e0216064 (2019).

154 DePas, W. H. *et al.* Exposing the three-dimensional biogeography and metabolic states of pathogens in cystic fibrosis sputum via hydrogel embedding, clearing, and rRNA labeling. *MBio* **7**, e00796-00716 (2016).
155 Chen, F., Tillberg, P. W. & Boyden, E. S. Expansion microscopy. *Science* **347**, 543-548 (2015).
156 Ku, T. *et al.* Multiplexed and scalable super-resolution imaging of three-dimensional protein localization in size-adjustable tissues. *Nature biotechnology* **34**, 973 (2016).
157 Albanese, A. & Chung, K. Neuroimaging: Whole-brain imaging reaches new heights (and lengths). *eLife* **5**, e13367 (2016).
158 Zhao, Y. *et al.* Nanoscale imaging of clinical specimens using pathology-optimized expansion microscopy. *Nature biotechnology* **35**, 757 (2017).
159 Chang, J.-B. *et al.* Iterative expansion microscopy. *Nature methods* **14**, 593 (2017).
160 Greenbaum, A. *et al.* Bone CLARITY: Clearing, imaging, and computational analysis of osteoprogenitors within intact bone marrow. *Sci Transl Med* **9**, doi:10.1126/scitranslmed.aah6518 (2017).
161 Michalski, M. N. & Williams, B. O. A quest for clarity in bone erosion: The role of sequestosome 1 in Paget's disease of bone. *J Biol Chem* **293**, 9542-9543, doi:10.1074/jbc.H118.003689 (2018).
162 Yin, M. T. & Overton, E. T. Increasing clarity on bone loss associated with antiretroviral initiation. *J Infect Dis* **203**, 1705-1707, doi:10.1093/infdis/jir184 (2011).
163 Li, W., Germain, R. N. & Gerner, M. Y. Multiplex, quantitative cellular analysis in large tissue volumes with clearing-enhanced 3D microscopy (Ce3D). *Proceedings of the National Academy of Sciences of the United States of America* **114**, E7321-E7330, doi:10.1073/pnas.1708981114 (2017).
164 Lagerweij, T. *et al.* Optical clearing and fluorescence deep-tissue imaging for 3D quantitative analysis of the brain tumor microenvironment. *Angiogenesis* **20**, 533-546 (2017).
165 Sylwestrak, E. L., Rajasethupathy, P., Wright, M. A., Jaffe, A. & Deisseroth, K. Multiplexed intact-tissue transcriptional analysis at cellular resolution. *Cell* **164**, 792-804 (2016).
166 Jensen, K. H. & Berg, R. W. CLARITY-compatible lipophilic dyes for electrode marking and neuronal tracing. *Sci Rep* **6**, 32674, doi:10.1038/srep32674 (2016).
167 Cronan, M. R. *et al.* CLARITY and PACT-based imaging of adult zebrafish and mouse for whole-animal analysis of infections. *Dis Model Mech* **8**, 1643-1650, doi:10.1242/dmm.021394 (2015).
168 Rocha, M. D. *et al.* Tissue clearing and light sheet microscopy: imaging the unsectioned adult zebra finch brain at cellular resolution. *Frontiers in neuroanatomy* **13**, 13 (2019).
169 Boutin, M. E. *et al.* A high-throughput imaging and nuclear segmentation analysis protocol for cleared 3D culture models. *Scientific reports* **8**, 11135 (2018).
170 Kurihara, D., Mizuta, Y., Sato, Y. & Higashiyama, T. ClearSee: a rapid optical clearing reagent for whole-plant fluorescence imaging. *Development* **142**, 4168-4179 (2015).
171 Palmer, W. *et al.* (2015).

172 McConnell, G. & Amos, W. B. Application of the Mesolens for subcellular resolution imaging of intact larval and whole adult Drosophila. *Journal of microscopy* **270**, 252-258 (2018).
173 Konno, A. & Okazaki, S. Aqueous-based tissue clearing in crustaceans. *Zoological letters* **4**, 13 (2018).
174 Luo, W. *et al.* Investigation of Postnatal Craniofacial Bone Development with Tissue Clearing-Based Three-Dimensional Imaging. *Stem Cells and Development* **28**, 1310-1321 (2019).
175 Nagababu, E. & Rifkind, J. M. Formation of fluorescent heme degradation products during the oxidation of hemoglobin by hydrogen peroxide. *Biochemical and biophysical research communications* **247**, 592-596 (1998).
176 Korytowski, W. & Sarna, T. Bleaching of melanin pigments. Role of copper ions and hydrogen peroxide in autooxidation and photooxidation of synthetic dopa-melanin. *Journal of Biological Chemistry* **265**, 12410-12416 (1990).
177 ITO, S. & WAKAMATSU, K. Chemical degradation of melanins: application to identification of dopamine‐melanin. *Pigment cell research* **11**, 120-126 (1998).
178 Manicam, C. *et al.* Effective melanin depigmentation of human and murine ocular tissues: an improved method for paraffin and frozen sections. *PloS one* **9**, e102512 (2014).
179 Schnell, S. A., Staines, W. A. & Wessendorf, M. W. Reduction of lipofuscin-like autofluorescence in fluorescently labeled tissue. *Journal of Histochemistry & Cytochemistry* **47**, 719-730 (1999).
180 Neumann, M. & Gabel, D. Simple method for reduction of autofluorescence in fluorescence microscopy. *Journal of Histochemistry & Cytochemistry* **50**, 437-439 (2002).
181 Yang, J. *et al.* Quenching autofluorescence in tissue immunofluorescence. *Wellcome Open Research* **2** (2017).
182 Callis, G. & Sterchi, D. Decalcification of bone: literature review and practical study of various decalcifying agents. Methods, and their effects on bone histology. *Journal of histotechnology* **21**, 49-58 (1998).
183 Schrijver, W. A. *et al.* Influence of decalcification procedures on immunohistochemistry and molecular pathology in breast cancer. *Modern Pathology* **29**, 1460 (2016).
184 Hatta, H. *et al.* A simple and rapid decalcification procedure of skeletal tissues for pathology using an ultrasonic cleaner with D-mannitol and formic acid. *Acta histochemica* **116**, 753-757 (2014).
185 Lei, Y., Grover, A., Sinha, A. & Vyavahare, N. Efficacy of reversal of aortic calcification by chelating agents. *Calcified tissue international* **93**, 426-435 (2013).
186 Grimm, J. B. *et al.* A general method to fine-tune fluorophores for live-cell and in vivo imaging. *Nature methods* **14**, 987 (2017).
187 Liu, A. K. L. *et al.* Bringing CLARITY to the human brain: visualization of Lewy pathology in three dimensions. *Neuropathology and applied neurobiology* **42**, 573-587 (2016).
188 Morawski, M. *et al.* Developing 3D microscopy with CLARITY on human brain tissue: Towards a tool for informing and validating MRI-based histology. *Neuroimage* **182**, 417-428 (2018).
189 Lai, H. M. *et al.* Next generation histology methods for three-dimensional imaging of fresh and archival human brain tissues. *Nature communications* **9**, 1066 (2018).

190 Hildebrand, S., Schueth, A., Herrler, A., Galuske, R. & Roebroeck, A. Scalable Labeling for Cytoarchitectonic Characterization of Large Optically Cleared Human Neocortex Samples. *Scientific reports* **9**, 1-10 (2019).
191 Moreno-Garcia, A., Kun, A., Calero, O., Medina, M. & Calero, M. An Overview of the Role of Lipofuscin in Age-Related Neurodegeneration. *Front Neurosci* **12**, 464, doi:10.3389/fnins.2018.00464 (2018).
192 Monnier, V. M., Kohn, R. R. & Cerami, A. Accelerated age-related browning of human collagen in diabetes mellitus. *Proceedings of the National Academy of Sciences* **81**, 583-587 (1984).
193 Power, R. M. & Huisken, J. Adaptable, illumination patterning light sheet microscopy. *Scientific reports* **8**, 9615 (2018).
194 Strobl, F., Schmitz, A. & Stelzer, E. H. Improving your four-dimensional image: traveling through a decade of light-sheet-based fluorescence microscopy research. *Nature protocols* **12**, 1103 (2017).
195 Andilla, J. *et al.* Imaging tissue-mimic with light sheet microscopy: A comparative guideline. *Scientific reports* **7**, 44939 (2017).
196 Power, R. M. & Huisken, J. A guide to light-sheet fluorescence microscopy for multiscale imaging. *Nature methods* **14**, 360 (2017).
197 Chen, B.-C. *et al.* Lattice light-sheet microscopy: imaging molecules to embryos at high spatiotemporal resolution. *Science* **346**, 1257998 (2014).
198 Mayer, J., Robert-Moreno, A., Sharpe, J. & Swoger, J. Attenuation artifacts in light sheet fluorescence microscopy corrected by OPTiSPIM. *Light: Science & Applications* **7**, 70 (2018).
199 Glaser, A. K. *et al.* Multi-immersion open-top light-sheet microscope for high-throughput imaging of cleared tissues. *bioRxiv*, 548107 (2019).
200 Wang, F. *et al.* Light-sheet microscopy in the near-infrared II window. *Nature methods* **16**, 545 (2019).
201 Piksarv, P. *et al.* Integrated single-and two-photon light sheet microscopy using accelerating beams. *Scientific reports* **7**, 1435 (2017).
202 Royer, L. A. *et al.* Adaptive light-sheet microscopy for long-term, high-resolution imaging in living organisms. *Nature biotechnology* **34**, 1267 (2016).
203 Royer, L. A., Lemon, W. C., Chhetri, R. K. & Keller, P. J. A practical guide to adaptive light-sheet microscopy. *Nature protocols* **13**, 2462 (2018).
204 Ryan, D. P. *et al.* Automatic and adaptive heterogeneous refractive index compensation for light-sheet microscopy. *Nature communications* **8**, 612 (2017).
205 Voigt, F. F. *et al.* The mesoSPIM initiative: open-source light-sheet mesoscopes for imaging in cleared tissue. *BioRxiv*, 577122 (2019).
206 Schindelin, J. *et al.* Fiji: an open-source platform for biological-image analysis. *Nature methods* **9**, 676 (2012).
207 Rueden, C. T. *et al.* ImageJ2: ImageJ for the next generation of scientific image data. *BMC bioinformatics* **18**, 529 (2017).
208 Quan, T. *et al.* NeuroGPS-Tree: automatic reconstruction of large-scale neuronal populations with dense neurites. *Nature methods* **13**, 51 (2016).
209 Jan, B. *et al.* Deep learning in big data Analytics: A comparative study. *Computers & Electrical Engineering* (2017).
210 Dean, J. *et al.* in *Advances in neural information processing systems.* 1223-1231.
211 Cui, H., Ganger, G. R. & Gibbons, P. B. Scalable deep learning on distributed GPUs with a GPU-specialized parameter server. *CMU PDL Technical Report (CMU-PD L-15-107)* (2015).

212 Pop, D. Machine learning and cloud computing: Survey of distributed and saas solutions. *arXiv preprint arXiv:1603.08767* (2016).
213 Chen, J. & Ran, X. Deep learning with edge computing: A review. *Proceedings of the IEEE* **107**, 1655-1674 (2019).
214 Kalimuthu, S., Jeong, J. H., Oh, J. M. & Ahn, B.-C. Drug discovery by molecular imaging and monitoring therapy response in lymphoma. *International journal of molecular sciences* **18**, 1639 (2017).
215 Bengel, F. M. & Gambhir, S. S. (Springer, 2005).
216 Fox, R. G. *et al.* Image-based detection and targeting of therapy resistance in pancreatic adenocarcinoma. *Nature* **534**, 407-411, doi:10.1038/nature17988 (2016).
217 Jones, M. R., Seeman, N. C. & Mirkin, C. A. Nanomaterials. Programmable materials and the nature of the DNA bond. *Science* **347**, 1260901, doi:10.1126/science.1260901 (2015).
218 Wang, P., Meyer, T. A., Pan, V., Dutta, P. K. & Ke, Y. The beauty and utility of DNA origami. *Chem* **2**, 359-382 (2017).
219 Wagenbauer, K. F., Sigl, C. & Dietz, H. Gigadalton-scale shape-programmable DNA assemblies. *Nature* **552**, 78-83, doi:10.1038/nature24651 (2017).
220 Sun, W. *et al.* Casting inorganic structures with DNA molds. *Science* **346**, 1258361, doi:10.1126/science.1258361 (2014).
221 Jiang, Q. *et al.* A self‐assembled DNA origami‐gold nanorod complex for cancer theranostics. *Small* **11**, 5134-5141 (2015).
222 Kuzyk, A. *et al.* DNA-based self-assembly of chiral plasmonic nanostructures with tailored optical response. *Nature* **483**, 311-314, doi:10.1038/nature10889 (2012).
223 Huang, Y., Huang, W., Chan, L., Zhou, B. & Chen, T. A multifunctional DNA origami as carrier of metal complexes to achieve enhanced tumoral delivery and nullified systemic toxicity. *Biomaterials* **103**, 183-196 (2016).
224 Derr, N. D. *et al.* Tug-of-war in motor protein ensembles revealed with a programmable DNA origami scaffold. *Science* **338**, 662-665, doi:10.1126/science.1226734 (2012).
225 Nickels, P. C. *et al.* Molecular force spectroscopy with a DNA origami-based nanoscopic force clamp. *Science* **354**, 305-307, doi:10.1126/science.aah5974 (2016).
226 Langecker, M. *et al.* Synthetic lipid membrane channels formed by designed DNA nanostructures. *Science* **338**, 932-936, doi:10.1126/science.1225624 (2012).
227 Jungmann, R. *et al.* Multiplexed 3D cellular super-resolution imaging with DNA-PAINT and Exchange-PAINT. *Nat Methods* **11**, 313-318, doi:10.1038/nmeth.2835 (2014).
228 Li, S. *et al.* A DNA nanorobot functions as a cancer therapeutic in response to a molecular trigger in vivo. *Nature biotechnology* **36**, 258 (2018).
229 Gopinath, A., Miyazono, E., Faraon, A. & Rothemund, P. W. Engineering and mapping nanocavity emission via precision placement of DNA origami. *Nature* **535**, 401-405, doi:10.1038/nature18287 (2016).
230 Yang, Y. *et al.* Self-assembly of size-controlled liposomes on DNA nanotemplates. *Nat Chem* **8**, 476-483, doi:10.1038/nchem.2472 (2016).
231 Knudsen, J. B. *et al.* Routing of individual polymers in designed patterns. *Nat Nanotechnol* **10**, 892-898, doi:10.1038/nnano.2015.190 (2015).

232 Ke, Y., Lindsay, S., Chang, Y., Liu, Y. & Yan, H. Self-assembled water-soluble nucleic acid probe tiles for label-free RNA hybridization assays. *Science* **319**, 180-183, doi:10.1126/science.1150082 (2008).
233 Douglas, S. M., Bachelet, I. & Church, G. M. A logic-gated nanorobot for targeted transport of molecular payloads. *Science* **335**, 831-834, doi:10.1126/science.1214081 (2012).
234 Praetorius, F. *et al.* Biotechnological mass production of DNA origami. *Nature* **552**, 84-87, doi:10.1038/nature24650 (2017).
235 Jiang, Q. *et al.* DNA origami as a carrier for circumvention of drug resistance. *Journal of the American Chemical Society* **134**, 13396-13403 (2012).
236 Chen, Z. Y. *et al.* Advance of molecular imaging technology and targeted imaging agent in imaging and therapy. *Biomed Res Int* **2014**, 819324, doi:10.1155/2014/819324 (2014).
237 Shroff, G. S. *et al.* Targeted Therapy and Imaging Findings. *J Thorac Imaging* **32**, 313-322, doi:10.1097/RTI.0000000000000294 (2017).
238 Yankeelov, T. E., Abramson, R. G. & Quarles, C. C. Quantitative multimodality imaging in cancer research and therapy. *Nat Rev Clin Oncol* **11**, 670-680, doi:10.1038/nrclinonc.2014.134 (2014).
239 Pan, C. *et al.* Shrinkage-mediated imaging of entire organs and organisms using uDISCO. *Nature Methods* **13**, 859-867, doi:10.1038/nmeth.3964 (2016).
240 Cai, R. *et al.* Panoptic imaging of transparent mice reveals whole-body neuronal projections and skull-meninges connections. *Nat Neurosci* **22**, 317-327, doi:10.1038/s41593-018-0301-3 (2019).
241 Pan, C. *et al.* Deep Learning Reveals Cancer Metastasis and Therapeutic Antibody Targeting in the Entire Body. *Cell* **179**, 1661-1676 e1619, doi:10.1016/j.cell.2019.11.013 (2019).
242 Heumann, D. & Roger, T. Initial responses to endotoxins and Gram-negative bacteria. *Clin Chim Acta* **323**, 59-72, doi:10.1016/s0009-8981(02)00180-8 (2002).
243 Agarwal, N. P., Matthies, M., Gür, F. N., Osada, K. & Schmidt, T. L. Block copolymer micellization as a protection strategy for DNA origami. *Angewandte Chemie International Edition* **56**, 5460-5464 (2017).
244 Paul, S. M. *et al.* How to improve R&D productivity: the pharmaceutical industry's grand challenge. *Nature Reviews Drug Discovery* **9**, 203-214, doi:10.1038/nrd3078 (2010).
245 Lindner, J. R. & Link, J. Molecular Imaging in Drug Discovery and Development. *Circ Cardiovasc Imaging* **11**, e005355, doi:10.1161/CIRCIMAGING.117.005355 (2018).
246 Li, S. *et al.* A DNA nanorobot functions as a cancer therapeutic in response to a molecular trigger in vivo. *Nature Biotechnology* **36**, 258-264, doi:10.1038/nbt.4071 (2018).
247 Jiang, D. *et al.* Multiple-Armed Tetrahedral DNA Nanostructures for Tumor-Targeting, Dual-Modality in Vivo Imaging. *ACS Appl Mater Interfaces* **8**, 4378-4384, doi:10.1021/acsami.5b10792 (2016).
248 Zhang, Q. *et al.* DNA origami as an in vivo drug delivery vehicle for cancer therapy. *ACS nano* **8**, 6633-6643 (2014).
249 Lee, H. *et al.* Molecularly self-assembled nucleic acid nanoparticles for targeted in vivo siRNA delivery. *Nat Nanotechnol* **7**, 389-393, doi:10.1038/nnano.2012.73 (2012).

250 Zhu, G. *et al.* Intertwining DNA-RNA nanocapsules loaded with tumor neoantigens as synergistic nanovaccines for cancer immunotherapy. *Nature communications* **8**, 1-13 (2017).
251 Baig, M., Babar, U., Arshad, U. & Ullah, M. A. DNA Origami and Bionanotechnology: An efficacious tool for modern therapeutics and drug delivery. *International Journal of Development Research* **8**, 24660-24669 (2018).
252 Jiang, Q., Liu, S., Liu, J., Wang, Z. G. & Ding, B. Rationally Designed DNA-Origami Nanomaterials for Drug Delivery In Vivo. *Adv Mater* **31**, e1804785, doi:10.1002/adma.201804785 (2019).
253 Ramakrishnan, S., Ijas, H., Linko, V. & Keller, A. Structural stability of DNA origami nanostructures under application-specific conditions. *Comput Struct Biotechnol J* **16**, 342-349, doi:10.1016/j.csbj.2018.09.002 (2018).

ACKNOWLEDGEMENTS

I am very grateful to write the last part of my thesis, acknowledgements, as the summary of my fruitful PhD life not only covering the scientific work but also the after-work explores. Recalling the beginning of PhD study, I was so excited and enthusiastic to the new adventures in new research areas and new environments. At this point, I would like to express my sincere gratitude to Dr. Ali Ertürk who gave me the opportunity of studying in an international team with diverse background members. His ambitious views in scientific achievements encouraged and inspired me to complete my projects and his guidance helped me in the research. Many Thanks to you!

With this thesis, I give all my thanks to lab members and collaborators, without whom I cannot come to the ending of long PhD journey. Mr. Mihail Ivilinov Todorov and I were enrolled in LMU at the same year. He is always available for me to give his professional support, suggestion, knowledge and idea during the whole process of research, also, we explored numbers of hiking routes around Munich to enjoy the beautiful life of fresh air, greens, sunshine and wind. Ruiyao (Marika) Cai is not only an intelligent colleague but also a whole-life friend for me. I appreciate her patience, her honesty, her generous and her independency. She gave me lots of help and strong supports when I faced difficulties in the work and life. There are so many beautiful memories with everyone in the daily work and collaboration, I cannot describe one by one. All in all, I would like to thank Dr. Chenchen Pan, Dr. Doris Kalternecker, Dr. Benjamin Förstera, Dr. Karen Stanic Aguilera, Dr. Harsharan Singh Bhatia, Dr. Rupinde Kaur, Dr. Tzu-lun Wang, Mr. Rami AI-Maskari, Mr. Hongcheng Mai, Mr. Zhouyi Rong, Miss Müge Molbay, Miss Ilgin Kolabas, Mrs Ana Toman, Mr. Marin Bralo, Dr. Hanno Steinke, Dr. Elisabeth Kemter, Dr. Benjamin Kick, Mr. Alireza Ghasemi, Dr. Oliver Schoppe, Mr. Johannes Christian Paetzold, Dr. Stefan Roth, Dr. Vikramjeet Singh, Dr. Mathias Hübner, Mr. Martin Warmer, Dr. Arnaldo Parra-Damas, Dr. Benno Gesierich, Mr. Milagros N. Wong, Mr. Tobias B. Huber. Miss Lina Paulenz, Miss Madita Reimer, Dr. Chongyue Zhao for their continuous and kind help.

My sincere thanks also goes to my Thesis Advisory Committee (TAC) members: Prof. Dr. Jürgen Bernhagen, Prof. Dr. Christian Haass, Dr. Ali Ertürk, Prof. Dr. Hendrik Dietz, Dr. Oliver Thorn Seshold, for their insightful comments and encouragements, also for the critical questions which incented me to widen my research from various perspectives. Specially, I am greatly appreciate that Prof. Dr. Jürgen Bernhagen carefully revised my thesis and gave valuable comments and inputs. Besides, I would like to thank my collaboration advisors: Prof. Dr. Ingo Bechmann, Prof. Dr. Eckhard Wolf, Prof. Dr. Jan Lipfert, Dr. Oliver Thomas Bruns,

Prof. Dr. Marco Düring, Dr. Arthur Liesz, Dr. Victor Puelles Rodriguez for their attentive guidance and supports.

With a special mention to the Institute of Stroke and Dementia, where provided me an open, free, comfortable and scientific working environment and gave access to the laboratory, research facilities and animal facilities. Without the whole precious and systematic supports it would not be possible to conduct this research. To my enrolling Munich Medical Research School (MMRS), it was fantastic to have the opportunity to conduct my PhD under its great organization.

A very special gratitude goes out to all friends. Dr. Xiaokang Li, Dr. Meng Yang, Miss Xiaohan Leng, Miss Shaomiao Zeng, Mr. Chris Becker, Mr. Man Su et al. provided me through moral and emotional support in my life.

And finally, last but by no means least, I gave all my thanks and loves to my family for supporting me spiritually throughout the PhD and my life in general.

Thanks for all your encouragement!